NOTE TO USERS

MULTI-COMPONENT DEFECT MODEL

FOR SEMICONDUCTOR LASERS

By

SAMUEL KAR KIN LAM, B.Sc., M.Sc.

A Thesis

Submitted to the School of Graduate Studies

in Partial Fulfilment of the Requirements

for the Degree

Doctor of Philosophy

McMaster University

MULTI-COMPONENT DEFECT MODEL FOR SEMICONDUCTOR LASERS

DOCTOR OF PHILOSOPHY (2004) McMaster University

(Engineering Physics) Hamilton, Ontario

TITLE: Multi-component Defect Model for Semiconductor Lasers

AUTHOR: Samuel Kar Kin Lam, B.Sc. (University of Western Ontario)

M.Sc. (University of Waterloo)

SUPERVISOR: Professor D.T. Cassidy

NUMBER OF PAGES: xii, 116

ABSTRACT

A multi-component defect model for degradation in semiconductor lasers is derived, discussed, and compared to experimental data and other existing degradation models for semiconductor lasers. The degradation model was designed to describe the change of threshold current as a function of aging time and is based on a population growth model in which only limited resources for the creation or growth of defects exist. Besides degradation, defect-annealing effect is incorporated into the multi-component model to examine high-power lasers that exhibit an annealing effect. A compatible lifetime estimation scheme is derived, discussed, and compared to the Hartman-Dixon method [Appl. Phys. Lett. **26**, 239 (1975)] for lifetime estimation.

Photoluminescence topography was utilized to probe the surface stability of semiconductor lasers during aging. A degradation of photoluminescence yield was observed at the active region. The degradation signifies an increase of surface recombination velocity. However, the reflectance of the surface is not modified by the aging-induced photoluminescence degradation.

ACKNOWLEDGEMENTS

First, I would like to thank my supervisor, Prof. Daniel T. Cassidy, for his guidance and inspiration during the course of my study. I am grateful to have worked under his supervision in a dynamic research team. I would like to thank Dr. Douglas M. Bruce for the endless help in my experimental work and all the fun discussions in the lab. If research is a religion, then Doug is my saviour.

I would also like to thank my industrial supervisor, Dr. Robert E. Mallard, for his insightful suggestions and a lot of helpful discussions. The assistance from Optoelectronic Device Reliability and Testing Group of Bookham Technology in aging the laser samples is acknowledged.

I wish to thank Mark Fritz for being the best labmate I have ever had, Adam Densmore for being an excellent housemate and colleague, Luke Doran and Debbie Lisak for introducing me to the new lab. I also wish to thank Elvira Evangelista for all the hard work in helping me finish my thesis.

Thanks to my teachers, friends, and colleagues: Prof. A.H. Kitai, Prof. D.A. Thompson, Prof. P. Mascher, Prof. P.E. Jessop, A. Ait-Ouali, G. Letal, M. Boudreau, J. Wojcik, J. Hazell, E. Irving, P. Pace, G. Pearson, M. Pearson, T. Somerville, P. Waldron, D. Deforge, M. Hamp, G. Morrison, H. Wang, J. Wang, J. Welbourne, S. Woodworth, and A. Vandermeer.

Finally, I wish thank Jason Hinek, Tom Holly, Sean Showell, my parents, Sau-Ming and Lai-Hing, my brother, Stephen, my sister, Cora, my uncles, aunts, and their families, my wife, Kelly, for all the love, encouragement, and support.

TABLE OF CONTENTS

LIST OF FIGURES

LIST OF TABLES

CHAPTER 1. INTRODUCTION

Threshold current, operating current, and differential quantum efficiency are the parameters that are typically used to evaluate the performance of a laser diode. In this thesis, the threshold current is utilized as a primary source for studying the aging of laser diodes. In modeling the change of threshold current with aging time, the defect density was assumed to be the only variable that caused the observable change. The rate of growth of the defect density as a function of temperature is thought to be described by the Arrhenius relation, which allows one to predict the performance of devices at operating temperature based on the lifetest result at an elevated temperature. A lifetime estimation scheme is the heart of a reliability reassurance scheme, and is the practical application of any degradation models. The lifetime estimation scheme can be constructed using a threshold degradation model and the Arrhenius relation. The purpose of this thesis is to provide the reliability engineering community with a lifetime estimation scheme using a physical defect model that was conceived in this doctoral study.

This thesis is organized as follows. In Chapter 2, an expression for the change in threshold current of a semiconductor laser diode as a function of aging time under constant thermal and current aging is presented. The expression forms a sigmoidal shape with aging time, and is accurate in describing the increase of the threshold current during aging. In the case when nonlinearities or "knees" occur in the threshold current aging curve, a multi-component defect model is

utilized to explain the observation. This multi-component defect model allows multiple sigmoidal curves to be incorporated in the description. Each sigmoidal curve is thought to represent the growth of one type of defect complex. The parameters in the model are designed to have physical meaning corresponding to the properties of the laser material. The model is compared to five popular models used for describing the threshold current aging characteristics.

In Chapter 3, the change of threshold current of a semiconductor laser diode as a function of time under the influence of defect annealing is discussed. This new approach combines the analytical multi-component model (MCM) discussed in Chapter 2 and an annealing effect. The observable effect of the annealing on the threshold current is attributed to a reduction of the internal loss in the laser, α_i, as opposed to a reduction in the number of nonradiative recombination centers. The extended MCM is then utilized to compare with the experimental data that exhibit the intricate state when degradation and annealing co-exist in a semiconductor laser. Comparison with an existing defect annealing model is also presented.

In Chapter 4, the effects of the growth of two non-interacting populations of defects in the cavity of a semiconductor laser diode, induced by accelerated lifetesting, are presented. The development of one type of defect is considered to give rise to a particular failure mode or mechanism. Using a multi-component model (MCM), I demonstrate that the evolution of the threshold current as a function of time is strongly affected by the operating temperature. The

progression of the degradation in terms of different thermal activation energies associated with each of the different failure modes is described. This observation explains why a common shape of the aging curve is seldom observed from one experiment to another and why it is difficult to have one universal threshold-aging model that everyone agrees on. In addition, the study offers insight on the estimation of lifetime of a semiconductor laser diode.

In Chapter 5, a degradation of the photoluminescence from the $SiO_x/Si/SiO_x$ coated n-InP facet on a set of aged semiconductor lasers is reported using room-temperature spatially-resolved and time-resolved photoluminescence techniques. Unlike the photoluminescence from bulk InP, the photoluminescence from the $SiO_x/Si/SiO_x$ coated n-InP facet increases with illumination time. This enhanced photoluminescence was used as an indicator to monitor the facet quality during the aging of a device. A time evolution of the spatially-resolved photoluminescence measurements on the laser facet were recorded during the course of aging. A degradation of the enhanced photoluminescence yield over aging time was detected under the active region after aging. This degradation of the enhanced photoluminescence yield is concluded to signify an increase of surface recombination velocity due a weakened passivation effect.

Finally, a summary of this thesis is provided in chapter 6. Possible future works to extend the studies are also discussed.

CHAPTER 2. MULTI-COMPONENT DEFECT MODEL WITHOUT ANNEALING

2.1 INTRODUCTION

Threshold current (I_{th}) is frequently used as a figure of merit of the performance of a laser diode. In practice, researchers plot the threshold current as a function of aging time and extrapolate the result to estimate the lifetime of a device[1]. This extrapolation is often performed using an empirical formula[2] that has little physical meaning in its form (see Sec. 2.5 on the Sim model and Eq. (2.14)).

In this chapter, a model for the change of threshold current as a function of aging time in the wearout failure mode is described. The model combines Chuang's approach[3] with a classic population growth model, and arose from my suggestions and calculations. The important feature of the model is that it assumes that the rate of creation of defects or growth of defects does not continue unabated under a finite environment. If the change of threshold current is proportional to the change of defect population, then the rate of change of threshold current should saturate at a certain point in time during aging due to the saturation of the rate of growth of defects, which coincides with the general observations regarding gradual degradation.[4,5] Furthermore, it is suggested that there is more than one type of defect existing in lasers which can lead to an increase of the threshold current. These different types of defects are identified by their activation energy. I call this model a multi-component model (MCM) to

distinguish it from other models that I will compare it with. I chose the name, multi-component model, because it implies that there exists more than one type of defect.

2.2 AGING PROCESS

In estimating the lifetime of a device, it is a common practice to place the device under accelerated stress aging. The stress aging typically involves continuous operation of the device under elevated current and ambient temperature. The levels of bias current and temperature are chosen such that the devices under testing show an accelerated rate of degradation without the introduction of additional failure mechanisms. If the activation energy is known, then it is possible to estimate lifetime at room temperature from the lifetime measurement performed under stress aging[6].

The samples used in the study are ridge-waveguide strained multi-quantum-well gain-coupled distributed feedback (RWG MQW GC DFB) lasers, which have structure similar to the ones used by Lu *et al.*[7] The aging process that these lasers underwent involved running 150 mA of current through the laser in an oven at a controlled ambient temperature of 150 °C. During the course of aging, the output power-current-voltage (L-I-V) characteristics of the devices were periodically measured in an *ex-situ* station at room temperature (25 °C). The performance evaluation measurements were done more frequently at the

beginning of the aging process to provide resolution on the rapid degradation observed in the early stage of aging. Then the time between measurements was gradually moved further apart as the lasers were aged longer. Ten samples that were aged for 2074 hours were examined. These samples were selected from a group of aged samples based on the criterion that they all exhibited wearout failure, as opposed to catastrophic failures during aging. The aging and characterization of the samples were performed in a state-of-the-art industrial lifetesting laboratory.

2.3 CAUSES OF DEGRADATION

To build a mathematical description for a degradation model, it is important to understand how a semiconductor laser degrades. The degradation in semiconductor lasers is caused by the growth of dark line defects (DLDs) and dark spot defects (DSDs).[8] The formation of dark line defects takes place due to recombination enhanced defect motion[9] (REDM). In particular, REDM can be subdivided into recombination enhanced dislocation climb (REDC) and recombination enhanced dislocation glide (REDG). The purpose of this section is to illustrate the basic concepts of degradation mechanisms. Therefore, I will only show certain selected examples rather than provide an exhaustive list of all mechanisms.

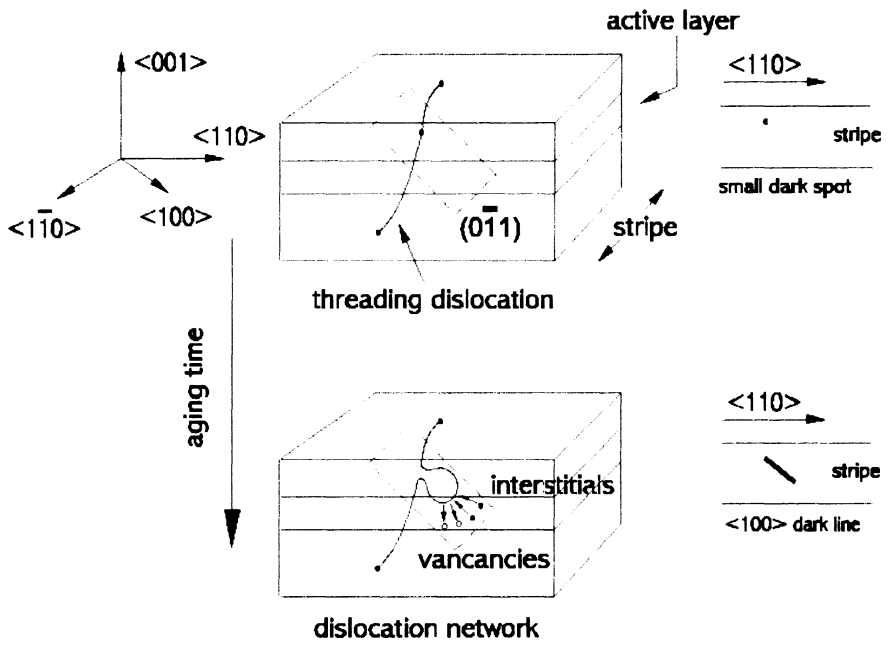

Fig. 2.1. Formation of <100> DLD during aging.[10]

An example illustrating the formation of a <100> DLD in AlGaAs/GaAs lasers[10] is given in Fig. 2.1. Normally, the growth of a <100> DLD requires a threading dislocation as a seed that is introduced during crystal growth as shown on the upper left diagram of Fig. 2.1. A threading dislocation in this case could be observed, using electroluminescence (EL) or photoluminescence (PL), as a dark spot defect (DSD) in the (001) plane of the active region. In the course of aging, the part of the threading dislocation in the active region starts to deform into a dislocation dipole in the $(0\,\bar{1}\,1)$ plane with the assistance of REDC. Further elongated distortion in the $(0\,\bar{1}\,1)$ plane extends a dislocation network from the dislocation dipole during aging. The name <100> DLD comes because if

someone was to observe the active region using EL or PL on the (001) plane, the dislocation network in the $(0\bar{1}1)$ plane would appear to be a dark line in the <100> direction as depicted on the lower right diagram of Fig. 2.1. There are two theoretical models for the growth of dislocations through REDC. These models describe the growth of dislocation through the absorption of interstitials at a dislocation[11] (extrinsic defect model) and the emission of vacancies at a dislocation[12] (intrinsic defect model), respectively. The true model of dislocation formation is still an open question. However, it is widely believed that the condensation of point defects with the momentum transfer from electron-hole recombinations is needed for the formation of dislocations.[13,14,15]

Another type of dislocations that is sometimes observed in degraded semiconductor lasers is <110> DLD. <110> DLD is normally generated by REDG with the assistance of residual strain.[16,17,18] Since formation of the defects requires electron-hole recombination, the exchange of interstitials and vancancies is believed to participate in the formation mechanism.[9] The ingredients of DSDs can be host atoms such as Ga in InGaAsP[19] or migrated metal such as Au[20] from the electrode. The formation of DSDs relies on electron-hole recombination, ambient temperature, strain field, and electric field.

The stress parameters for investigating degradation behaviour in semiconductor lasers generally involves elevated temperature and bias current, since they contribute some important factors for degradation mechanisms. Discussions about degradation due to strain can be found elsewhere.[21,22] The

important idea in this section to be presented to the reader is that the degradation mechanisms including the growth of DLDs and DSDs involves the segregation, coalescence, and exchange of interstitials and vacancies. In other words, the formation of the destructive secondary defect structure always requires certain primary sources as a fuel, which is analogous to the survival or growth of a population such as animals and plants in a finite system. Due to this reason, I formulated the rate of change of threshold with aging time according to a population growth model in a finite system.

2.4 DEFECT MODEL

My goal was to derive a simple and realistic expression that can describe the aging behavior of semiconductor lasers. Following Chuang's approach[3], I assumed that the change in threshold current, $\Delta I_{th}(t)$, is given by the change in the nonradiative recombination current, such that

$$\Delta I_{th}(t) = I_{nr}(t) - I_{nr}(0), \tag{2.1}$$

where

$$I_{nr}(t) = qVAN_d(t)n_{th}/\eta_i, \tag{2.2}$$

q is a single electron charge, V = wdL (width × thickness × length of the active region) is the volume of the active region, and η_i is the internal injection efficiency. AN_dn_{th} is the nonradiative carrier capture rate at the defects at

threshold with a defect density of N_d, a carrier density of n_{th}, and A is a nonradiative recombination rate. The carrier density for above threshold operation is assumed to be pinned at the threshold value n_{th}. Please note that N_d is the density of the nonradiative defect complexes in the active region, and these complexes will be referred to as defects.

The defect density N_d is modeled to increase as the diode ages. For the defect generation model, I assumed that the creation or growth of a type of defect requires certain types of resources, and that the resources are limited. Therefore, as the defect density N_d increases, the resources will be depleted, and the rate of degradation slows down as a result. This idea is similar to a model of population growth in a finite environment[23,24]. The resources for the creation and growth of the nonradiative recombination sites are identified as pre-existing defects that do not cause nonradiative recombination. It is assumed that this population of pre-existing defects is set during the manufacture of the device.

For the case of one type of defect in a cavity of volume V, the time rate of change of the number of defects, N(t), is given as

$$\frac{dN(t)}{dt} = K_n N(t) - C_n N(t)[N(t) - 1]. \tag{2.3}$$

where

$$K_n = \kappa np \exp\left(-\frac{E_a}{kT}\right) = \kappa n^2 \exp\left(-\frac{E_a}{kT}\right) \tag{2.4}$$

and

$$C_n = cnp\exp\left(-\frac{E_a}{kT}\right) = cn^2\exp\left(-\frac{E_a}{kT}\right). \quad (2.5)$$

The subscript n in K_n and C_n indicates that the parameters are a function of n, where n is the stress carrier density and is assumed to be constant with time in the constant current aging experiment. It is also assumed that the numbers of injected electrons and holes are equal, that is, n = p in the undoped active region. The first term of Eq. (2.3) can be thought of as the natural growth rate of the defect concentration and the second term can be thought of as the modification due to the environment. K_n and C_n, in unit of $hour^{-1}$, govern the rate of growth of the defect population and the rate of saturation of the defect population, respectively. The form of N(N-1) in the second term assumes that each defect competes with one other defect at a time, and there are N(N-1)/2 possible pairs of defects competing for the same finite resources. The idea of this pairing competition is illustrated in Fig. 2.2.

Due to this reason, the saturation factor in the second term in Eq. (2.3) is proportional to the number of possible pairs of competition. In Eqs. (2.4) and (2.5), E_a is the activation energy which is a property of the defect that characterizes the extent to which the defect reaction rate changes with temperature, k is the Boltzmann constant, T is the absolute temperature, and κ and c are constants. In general, κ and c can be thought of as the rate of utilization of resources for enhancing and suppressing growth respectively. Equation (2.4) contains the recombination-enhanced defect generation term, κnp, introduced by

Chuang *et al.*[3] Furthermore, Eq. (2.5) has the form of Eq. (2.4) to account for the inverse of the process in Eq. (2.4).

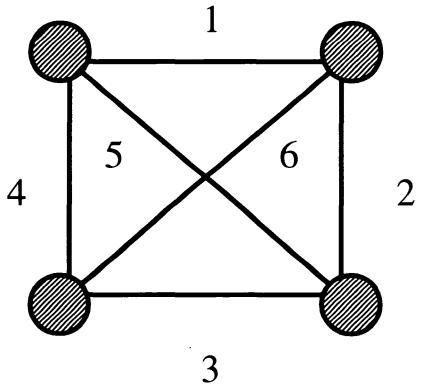

Number of defects N = 4

Number of possible pairs of interaction = N(N-1)/2 = 6

Fig. 2.2. An example of pairing interaction between 4 defects.

Eq. (2.3) can be written in terms of the defect density N_d by substituting $N=N_dV$ into the equation:

$$\begin{aligned}\frac{dN_d(t)}{dt} &= K_n N_d(t) - C_n N_d(t)[VN_d(t)-1] \\ &= [K_n + C_n]N_d(t)\left[1 - \frac{C_n V}{K_n + C_n} N_d(t)\right].\end{aligned} \tag{2.6}$$

The solution of this differential equation is (see Sec. 7.1 for derivation and notation):

$$N_d(t) = \frac{M_n N_d(0)}{N_d(0) + (M_n - N_d(0))\exp[-C_n V M_n t]} \tag{2.7}$$

The resulting defect density forms a sigmoidal curve with time. Please note that $N_d(\infty) = M_n = (\kappa + c)/(cV)$, which marks the maximum value for the defect density, is independent of carrier density, activation energy, and temperature. By substituting Eqs. (2.7) and (2.2) in Eq. (2.1), $\Delta I_{th}(t)$ becomes

$$\Delta I_{th}(t) = \frac{qVAn_{th}}{\eta_i}\left[\frac{M_n N_d(0)}{N_d(0) + (M_n - N_d(0))\exp[-C_n V M_n t]} - N_d(0)\right], \qquad (2.8)$$

Eq. (2.8) only describes the change of I_{th} under one type of defect. In principle, if there is more than one family of defect competing for the same resources, there are ς coupled non-linear differential equations for ς species:

$$\begin{aligned}
\frac{dN_{d1}(t)}{dt} &= N_{d1}(t)\left[a_{11} - a_{12}VN_{d1} - a_{13}VN_{d2} - \ldots - a_{1,\varsigma+1}VN_{d\varsigma}\right] \\
\frac{dN_{d2}(t)}{dt} &= N_{d2}(t)\left[a_{21} - a_{22}VN_{d1} - a_{23}VN_{d2} - \ldots - a_{2,\varsigma+1}VN_{d\varsigma}\right] \\
&\vdots \\
\frac{dN_{d\varsigma}(t)}{dt} &= N_{d\varsigma}(t)\left[a_{\varsigma 1} - a_{\varsigma 2}VN_{d1} - a_{\varsigma 3}VN_{d2} - \ldots - a_{\varsigma,\varsigma+1}VN_{d\varsigma}\right]
\end{aligned} \qquad (2.9)$$

This is the general form of Volterra's equation[25]. To solve for each type of defect N_{dm}, where $m = 1, 2, \ldots \varsigma$, requires numerical analysis of the system. Equations (2.9) can be simplified under the assumption that the growth of one type of defect N_{dm} does not greatly affect the growth of other types of defects N_{dj} where $j \neq m$. Using this non-interacting-defect assumption, where $a_{ij} = 0$, if $j \neq 1$ or $j \neq i + 1$, Eqs. (2.9) can be simplified to a solvable form as follows,

$$\begin{aligned}
\frac{dN_{d1}(t)}{dt} &= N_{d1}(t)[a_{11} - a_{12}VN_{d1}] \\
\frac{dN_{d2}(t)}{dt} &= N_{d2}(t)[a_{21} - a_{23}VN_{d2}] \\
&\vdots \\
\frac{dN_{d\varsigma}(t)}{dt} &= N_{d\varsigma}(t)[a_{\varsigma 1} - a_{\varsigma,\varsigma+1}VN_{d\varsigma}]
\end{aligned} \tag{2.10}$$

The solution of each $N_{d\varsigma}$ in Eq. (2.10) will be of the form shown in Eq. (2.7). Since the total N_d is just the sum of all $N_{d\varsigma}$, a more general equation for describing I_{th} degradation due to ς different types of non-interacting defects can be written as,

$$\Delta I_{th}(t) = \frac{qVAn_{th}}{\eta_i}\left[\sum_{m=1}^{\varsigma}\frac{M_{nm}N_{dm}(0)}{N_{dm}(0) + (M_{nm} - N_{dm}(0))\exp[-C_{nm}VM_{nm}t]} - N_{dm}(0)\right], \tag{2.11}$$

where $M_{nm} = a_{m,1}/(a_{m,m+1}V)$ is the maximum defect density for the m-th component. The rate of saturation of the defect density in the m-th component, $C_{nm} = a_{m,m+1} = cn^2\exp[-E_{am}/(kT)]$, is assumed to be independent of time such that $c_m = c$ (c is a constant). In other words, any pair of C_{nm}'s will be the same if they have the same activation energy E_{am}. In fact, if c_m's vary from component to component, then there exist two different components that have the same activation energy and different c_m's, owing to the degenerate nature of c_m in connection with E_{am}. The term $a_{m,1}$ is equal to $(\kappa_m + c)n^2\exp[-E_{am}/(kT)]$ as discussed in Eqs. (2.3), (2.4), and (2.5). Then, $M_{nm} = (\kappa_m + c)/(cV)$. Equation (2.11) is the final form of the MCM. The interpretation of the MCM is as

follows. Defects form and grow by consuming resources from their vicinity. The fastest growing defects deplete the resources around them the fastest, so they cease activity early and form the first "knee" in the aging curve. The other defects deplete their resources at different stages according to their speed of consumption (based on E_{am}, T, c_m, n, and M_{nm}). They form the other "knees" on the aging curve.

In Fig. 2.3, the two figures show the fitted results of an I_{th}-time curve using (a) a one-component (one type of defect) model and (b) a two-component (two types of defects) model. In the fit shown in Fig. 2.3, $I_{th}(0) = I_{th0}$ to provide the fitting of the offset, which is equal to the sum of spontaneous emission, Auger recombination, stimulated emission, and leakage currents. By inspection, one can see, in the dash-circled areas, that the latter fits better to the experimental results. To provide a quantitative measure, the quality of the fits was compared using an F-test on the two variances of the fit, S^2_{1-comp} and S^2_{2-comp}. The fit variances are computed as[26]

$$S^2 = \frac{1}{N-M}\sum_{i=1}^{N}[y(t_i) - y_c(t_i)]^2 , \qquad (2.12)$$

where N is the number of data points, M is the number of fit parameters, $y(t_i)$ are the aging data points, and $y_c(t_i)$ are the best fit estimates of the $y(t_i)$. If one fitting model is much better than the other fitting model, then there should be a statistically significant difference in the variance of the fit. The *f* factor, which is the ratio of the two fit variances, is given by:

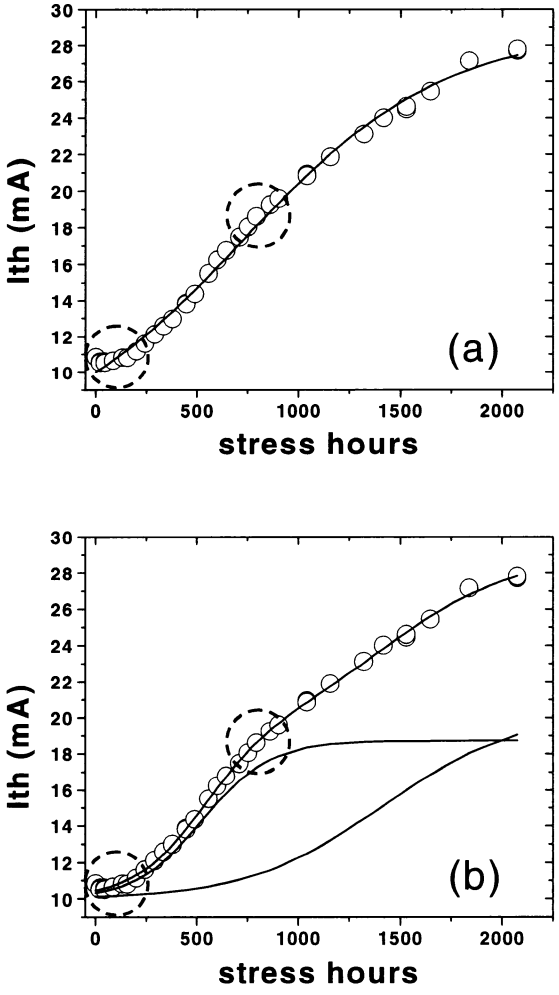

Fig. 2.3. Plots of threshold current as a function of aging time (circles: measured data; solid line: model) of a RWG MQW GC DFB laser labeled as Rb13: (a) the I_{th}-time curve fitted with a one-component (one type of non-radiative recombination sites) MCM; (b) the I_{th}-time curve fitted with a two-component (two types of non-radiative recombination sites) MCM. In (b), the first and second components of the best-fit line are also plotted below the data.

$$f = S^2_{1\text{-comp}} \Big/ S^2_{2\text{-comp}} = \frac{0.162}{0.024} = 6.75 . \quad (2.13)$$

The number of degrees of freedom in the one-component MCM case is 29, and the number of degrees of freedom in the two-component MCM case is 26. The critical value[27] in this case for a confidence level of 99% is 2.50. Thus there is a statistically significant difference between the fit variances and a two-component model is justified. The corresponding fitted parameters, tabulated in Table 2.1, are also very different between the two models. Please note that the uncertainties quoted in the table are standard deviations obtained from the error matrix multiplied by the standard deviation of the fit, $\sqrt{S^2}$. The MCM was fit to 9 other lasers using the two-component MCM. All the fit coefficients of the 10 lasers and the corresponding variances of the fit are tabulated in Table 2.2. Loosely speaking, a smaller variance of the fit indicates a better fit. It is found that the MCM fits well to all the lasers by comparing to the variances presented in Table 2.1. In Fig. 2.4, more examples of the fitted aging curves using the two-component MCM are presented. The fitted values of these examples can also be found in Table 2.2.

	Models	
Fit coefficients	One-component model	Two-component model
I_{th0} (mA)	5.35 ± 4.09	9.96 ± 0.26
Scaled $\frac{qV}{\eta_i} A n_{th}$ (mA-cm^3)	4.66 ± 0.62	1.07 ± 0.11
Scaled $c_1 n_{th}^2 V \exp\left(-\frac{E_{a1}}{kT}\right)$ (10^{-4} cm^3-hour^{-1})	3.89 ± 2.13	7.34 ± 2.05
Scaled M_1 (cm^{-3})	5.07 ± 1.17	8.14 ± 0.89
Scaled $N_{d1}(0)$ (cm^{-3})	1.00 ± 0.90	0.33 ± 0.25
Scaled $c_2 n_{th}^2 V \exp\left(-\frac{E_{a2}}{kT}\right)$ (10^{-4} cm^3-hour^{-1})	–	3.10 ± 0.34
Scaled M_2 (cm^{-3})	–	9.67 ± 1.15
Scaled $N_{d2}(0)$ (cm^{-3})	–	0.13 ± 0.12
Variance of fit, S^2	0.162	0.024
$f = S_{1-comp}^2 / S_{2-comp}^2$	0.162/0.024 = 6.75 > 2.50	

Table 2.1. List of the fitted parameters using one-component MCM and two-component MCM. Both cases were fitted using k = 8.62×10^{-5} eV/K and T = 423 K.

Samples	Rb02	Rb08	Rb10	Rb11	Rb13	Rb15	Rd03	Rd13	Rd20	Rd40
I_{th0} (mA)	11.40	9.76	9.38	11.46	9.96	11.71	14.82	10.85	11.83	16.79
$\frac{qV}{\eta_i} A n_{th}$ (mA-cm^3)	0.96	1.30	1.42	0.96	1.07	0.59	0.73	0.62	0.71	0.73
Scaled $cn_{th}^2 V \exp\left(-\frac{E_{a1}}{kT}\right)$ (10^{-4} cm^3-hour^{-1})	6.11	5.40	7.40	14.40	7.34	4.16	97.80	23.35	22.25	4.75
Scaled M_{n1} (cm^{-3})	9.73	8.79	7.35	4.25	8.14	11.47	1.94	3.19	3.67	9.93
Scaled $N_{d1}(0)$ (cm^{-3})	0.68	0.86	0.60	0.21	0.33	0.86	0.048	0.27	0.17	0.86
Scaled $cn_{th}^2 V \exp\left(-\frac{E_{a2}}{kT}\right)$ (10^{-4} cm^3-hour^{-1})	2.04	3.55	3.50	7.49	3.10	2.29	6.90	10.88	19.30	10.33
Scaled M_{n2} (cm^{-3})	14.01	8.17	8.13	4.54	9.67	11.46	5.09	3.05	1.85	2.08
Scaled $N_{d2}(0)$ (cm^{-3})	0.35	0.15	0.21	0.09	0.13	0.31	0.21	0.13	0.05	0.07
$M_{n2}/N_{d2}(0)$	40.03	54.47	38.71	50.44	74.38	36.97	24.24	23.46	37	29.71

Table 2.2. List of the fitted parameters for 10 RWG MQW GC DFB lasers. Please note that the uncertainties of the parameters in each laser are similar to the two-component MCM case in Table 2.1, and all cases were fitted using k = 8.62×10^{-5} eV/K and T = 423 K.

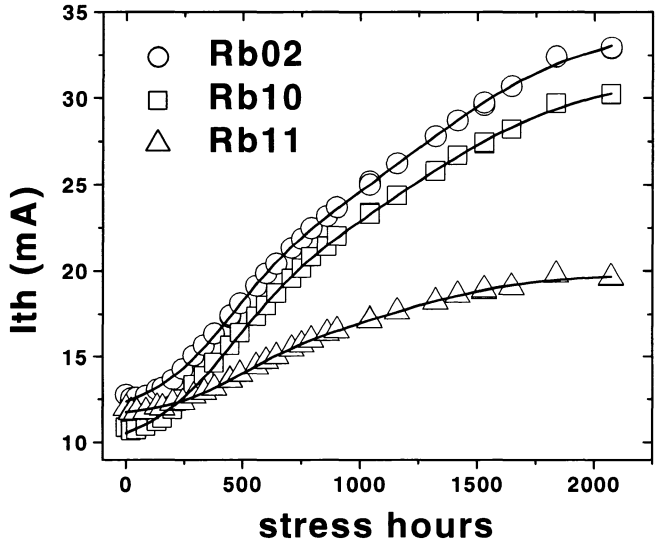

Fig. 2.4. Plot of three aging curves fitted with the two component MCM model.

2.5 COMPARISON

Five other types of expressions are considered in this section for comparison with the MCM in terms of disagreement in long-term saturation effect. I call them the Sim model, the Chuang model, the positive feedback model (PFM), the Imai model, and the extended defect model (EDM). The first model to examine is the Sim model, which is based on a heuristic approach. In the Sim model, the change of threshold current is given by[2],

$$\Delta I_{th}(t) = At^{n} \exp\left(-\frac{E_a}{kT}\right), \tag{2.14}$$

where A is a constant, t is the time normally measured in hours, n is the time exponent, E_a is the activation energy, k is the Boltzmann's constant, and T is the absolute temperature. This equation is used to predict the lifetime of a laser by fitting Eq. (2.14) to the I_{th}-time curve or the operating current aging data (I_{op}-time curve). One criterion in fitting data using this model is that the user needs to neglect the burn-in period which is, typically, the first 24 hours of aging at 125 °C operating temperature and 100 mA bias current[2]. Generally, the burn-in period increases as the stress temperature and the bias current decrease. In Fig. 2.5, the plot shows the fitting of the experimental data from Fig. 2.3 using the Sim model assuming the burn-in period equal to 44 hours. The corresponding fitting parameters are recorded in Table 2.3. One can easily observe that the Sim model has three weaknesses: (A) it cannot describe the I_{th}-time curve in the early aging stage (burn-in period); (B) it cannot explain the origin of the nonlinearities ("knees") observed in the curves; and, (C) no physical explanations on the shape of the I_{th}-time curve are given. The MCM gives better solutions to the problems in (A), (B), and (C) than any models I know of.

In practice, many researchers use linear extrapolation to predict the lifetime of a laser[1] using a known activation energy. In other words, they assume n = 1 in Eq. (2.14). This assumption makes the model more sensitive to the initial condition, and more likely to overestimate the threshold current degradation.

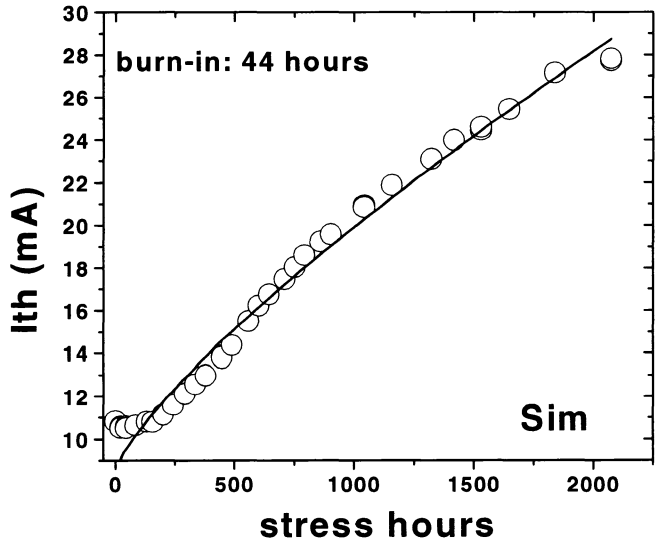

Fig. 2.5. Plot of Ith-time curve fitted by the Sim model. The fitting of the model neglects the aging data in the first 44 hours.

The next model to compare is the Chuang model. The Chuang model, the PFM, and the Imai model are very similar: they all contain an exponential function and predict an exponential growth in the defect density. At threshold, the Chuang model can be written as[3]

$$\Delta I_{th}(t) = I_{nr0}\{\exp[K_{th0}\, t \exp(-E_a/(kT))] - 1\} \tag{2.15}$$

where $I_{nr0} = I_{th0} - I_{sp}$ = constant.

The PFM contains two sub-models. One sub-model contains an exponential function while the other one contains a cosh function. I examine the exponential function since the cosh model has a similar nature. The PFM states that the concentration of the deep-level defects, N_l, is given as[28],

Sim model		Chuang model		EDM	
Fit coefficients	Values	Fit coefficients	Values	Fit coefficients	Values
I_{th0}	8.54±0.38	I_{th0}	9.22±0.14	I_{th0}	7.17±0.25
$A\exp\left(-\frac{E_a}{kT}\right)$	4.97×10^{-2} $\pm0.64\times10^{-2}$	I_{nr0}	1.20±0.08	$I_{th1}R$	0
n	0.787 ±0.003	$K_{th0}\exp\left(-\frac{E_a}{kT}\right)$	2.98×10^{-3} $\pm0.02\times10^{-3}$	$I_{th1}\Delta I_{th0}$	28.29 ±0.41
Burn-in	44 hours			$1/t_s$	6.4×10^{-4} $\pm0.3\times10^{-4}$
S^2	0.394	S^2	0.030	S^2	0.049

Table 2.3. The fitted parameters of the Sim model assuming burn-in period equal to 44 hours, the Chuang model, and the EDM.

$$N_l = N_{ls}\exp[K_f t]$$

where

$$K_f = C_{f,l}N_{c,l}\sum_l D_{nr,l}np. \tag{2.16}$$

N_{ls} is the initial condition of N_l, $C_{f,l}$ is the formation constant of deep-level defects, $N_{c,l}$ is the concentration of a core defect for the formation of the deep-level defect "l", $D_{nr,l}$ is the nonradiative recombination coefficient per deep-level defect "l", and n and p are the electron and hole concentrations respectively. One can assume K_f to be constant with time. According to Eqs. (2.1) and (2.2), the threshold current in this case becomes,

$$\Delta I_{th}(t) = \frac{qVAn_{th}}{\eta_i} N_{ls}[\exp(K_f t) - 1]. \quad (2.17)$$

In principle, K_f varies with temperature according to the Arrhenius relation just like the Chuang model, in which case, Eqs. (2.15) and (2.17) have an identical form.

Similarly, Imai *et al.* suggested that the degradation rate of the deep-level emission, R_{dl}, to be[29]

$$R_{dl} = \frac{[P(t_2) - P(t_1)]}{P(t_1)(t_2 - t_1)} = \frac{[I_{th}(t_2) - I_{th}(t_1)]}{I_{th}(t_1)(t_2 - t_1)}, \quad (2.18)$$

where P is the intensity of deep level emission and I_{th} is the threshold current. R_{dl} is taken to be independent of time. If one assumes that the model is characterized by the following differential equation,

$$\frac{dI_{th}}{dt} = R_{dl} I_{th}, \quad (2.19)$$

then the Imai model is obtained,

$$\Delta I_{th} = I_{th0}[\exp(R_{dl} t) - 1]. \quad (2.20)$$

R_{dl} is believed to vary with temperature according to the Arrhenius relation. Therefore Eq. (2.20) is also identical to Eq. (2.15) in terms of its mathematical form. A plot using the Chuang model is presented in Fig. 2.6, and the fitting parameters are recorded in Table 2.3. Since the PFM and the Imai model are similar to the Chuang model in terms of the mathematical form, only one plot is shown in this case. In Fig. 2.6, one can see that the Chuang model fits well in the

early rapid degradation, due to the exponential term in Eq. (2.15). This confirms the results as shown in Chuang's paper[3]. But the model deviates in a different direction from the experimental data after approximately 700 hours. Please also note that when Kondo *et al.*[28] applied the PFM in their aging data, the model was

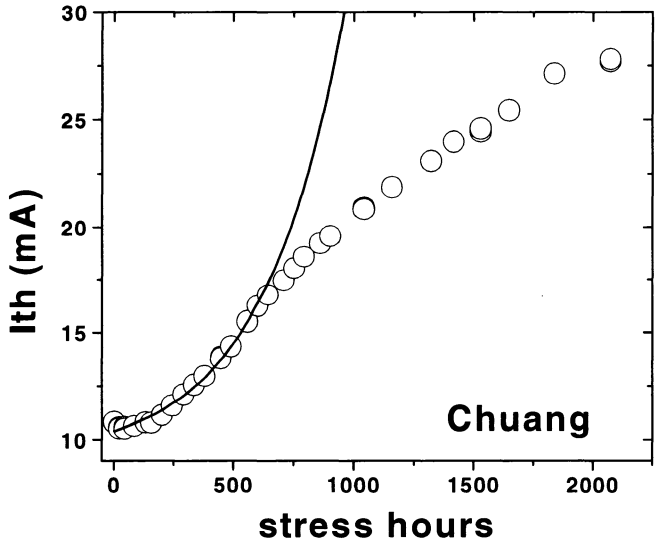

Fig. 2.6. Plot of I_{th}-time curve fitted by the Chuang model.

intended to apply to the aging curve after the first saturation beyond 3000 hours of aging. So strictly speaking, the PFM does not apply to the data presented in this thesis.

The last model I will discuss is the EDM. It has the closest form to the MCM. Assuming $\gamma' = \gamma$ (i.e. the capture rate at the accumulated defects in the p-n junction from the cladding layer is equal to the capture rate at the accumulated

defects in the p-n junction from the active region), the form of the threshold current is given as[30],

$$\Delta I_{th} = I_{th1}\{Rt + \Delta I_{th0}[1 - \exp(-t/t_s)]\}, \tag{2.21}$$

where I_{th1}, R, ΔI_{th0}, and t_s are treated as constants. In contrast to the MCM, the EDM always shows a positive growth in I_{th} due to the $I_{th1}Rt$ term in Eq. (2.21).

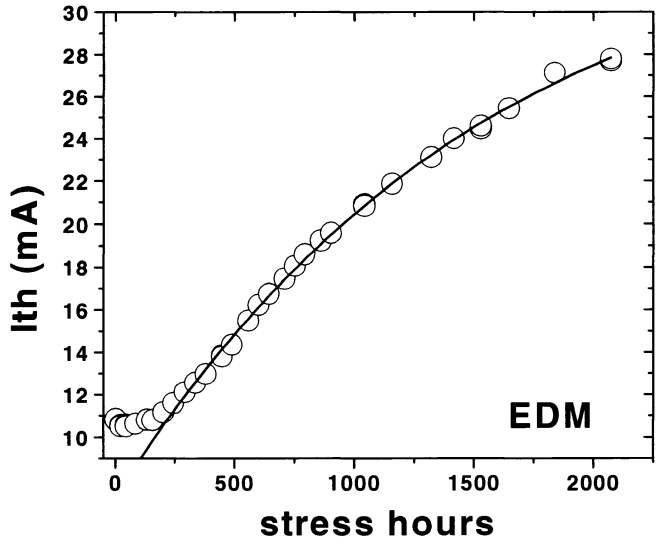

Fig. 2.7. Plot of I_{th}-time curve fitted by the EDM.

The form of Eq. (2.21) does not resemble the sigmoidal shape normally observed in the aging curve but it shows a partial saturation due to the term 1-exp(-t/t_s). Because of these reasons, the EDM will never come to a full saturation in terms of degradation and it cannot describe well the early stage of degradation. In Fig. 2.7, the plot shows a threshold current aging curve fitted by the EDM, and the fitting parameters are recorded in Table 2.3. The aging curve is fitted with the

second term of Eq. (2.21) equal to zero, because the linear term is used to describe long-term degradation[31] (beyond 2000 hours) and it causes the other fitting parameters to produce values that are not physical (e.g. out of possible boundary of the physical quantity) during fitting. That the EDM cannot fit well with the early rapid degradation in the first 100 hours of aging is evident in Fig. 2.7.

2.6 DISCUSSION

A correlation between the laser performance and the number of nonradiative recombination sites formed was observed. In the 10 lasers that were aged for 2074 hours, 4 of them are from a different quarter of the same wafer. From experience, the lasers from the Rb quarter degrade slower compared to the rest of the lasers from the Rd quarter. Fig. 2.8 shows a plot of 4 aging curves where 2 of them are from the Rb quarter and the other two are from the Rd quarter. The Rd lasers degrade slower compared to the Rb lasers. The fitted results of these four lasers can be found in Table 2.2. The explanation provided by the MCM from the fitting results in Table 2.2 lies in the difference in the maximum number of nonradiative recombination sites formed. Since only the second component of the two-component model determines the lifetime of the device, the maximum defect density of the second component M_2 in the two-component case and the corresponding initial defect density $N_2(0)$ were utilized.

To compare the devices in terms of M_2 and $N_2(0)$, the ratio of $M_2/N_2(0)$ was calculated. It is a necessary procedure, because both M_2 and $N_2(0)$ are scaled

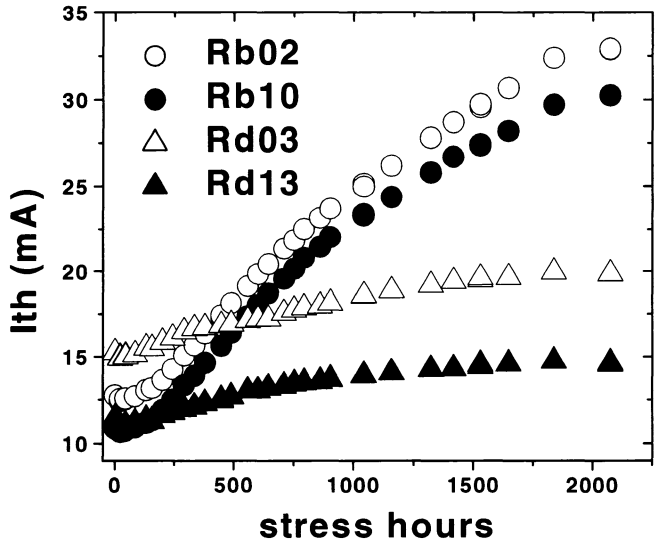

Fig. 2.8. Plot of the aging curve of the 4 lasers from two groups Rb and Rd respectively. The group Rb is marked with circles and the group Rd is marked with triangles.

quantities and different devices may be scaled with different values due to cancellation of common factors in Eq. (2.11). The initial defect density, $N_2(0)$, should be nominally the same for all devices, since they were grown on the same wafer. Then, the ratio $M_2/N_2(0)$ will allow the devices to be compared in terms of defect density. The average value of $M_2/N_2(0)$ in Rb is $\overline{X}_{Rb} = 49.17$ with a sample standard deviation, $S_{Rb} = 14.19$, and sample size, $N_{Rb} = 6$, while for Rd,

$\overline{X}_{Rd} = 28.60$, $S_{Rd} = 6.25$, and $N_{Rd} = 4$. A *t*-test can be used to test if the mean value of $M_2/N_2(0)$ for Rb lasers is larger than that for Rd lasers[32]:

$$t = \frac{\overline{X}_{Rb} - \overline{X}_{Rd}}{S_p \sqrt{\frac{1}{N_{Rb}} + \frac{1}{N_{Rd}}}} \qquad (2.22)$$

where

$$S_p^2 = \frac{(N_{Rb} - 1)S_{Rb}^2 + (N_{Rd} - 1)S_{Rd}^2}{N_{Rb} + N_{Rd} - 2}.$$

The *t* ratio, in this case, is 2.69. At 97.5% confidence level, the corresponding critical value for a one-tail Student's *t*-test with the number of degrees of freedom, $N_1+N_2-2 = 8$, is 2.306. Since the *t* ratio, 2.69, is larger than the critical value, 2.306, the $M_2/N_2(0)$ of Rb lasers is larger than the $M_2/N_2(0)$ of Rd lasers at > 97.5% confidence level. In other words, it appears that Rb lasers have more nonradiative recombination sites formed during aging compared to Rd lasers, assuming that the initial defect densities for both Rb and Rd lasers are the same. The rate at which the nonradiative recombination sites multiply varies as a function of the availability of the pre-existing resources for the growth of defect. The magnitude of M_2 physically represents the size of the defect multiplication resource pool. This idea of saturable degradation is equivalent to the idea that the degradation of light-emitting diodes depends on the number of pre-existing defects[33] where the pre-existing defects are equivalent to the pre-existing resources in our case. Please note that this comparison is performed under the assumption that the defect-annealing effect does not alter the comparison result,

since all lasers in this study are influenced by nominally an equal amount of annealing effect.

2.7 CONCLUSION

An analytical expression for threshold current of a semiconductor laser diode as a function of aging time in the wearout failure mode with saturable threshold current degradation is presented. Comparison of this model with other existing models as they apply to aging data confirms that the MCM indeed provides a more accurate description of the aging curve, since most models are not designed for saturable long-term degradation. More importantly, the parameters that are used in the model have well-defined physical interpretations, so users can understand the physics by fitting the model to I_{th}-time data. It can be applied to DFB lasers or other lasers that contains a resonant cavity. The burn-in period is not discarded in the analysis using the MCM model. The "knees" seen in the I_{th}-time curve are explained as signs of the saturation of the growth of the corresponding type of defects or nonradiative recombination sites. Furthermore, it is confirmed, based on a sample size of 10 lasers with > 97.5% confidence, that laser performance as measured by the threshold current is indeed limited by the number of pre-existing defects.

CHAPTER 3. EFFECTS OF ANNEALING ON DEGRADATION

3.1 INTRODUCTION

The MCM describes the aging behaviour in terms of multiple degradation modes with different rates of reaction.[34] This MCM takes into account depletion of raw material for growth of nonradiative recombination defects, and thus shows saturation in the change of threshold current, ΔI_{th}, with time. It is evident that processes by which defects such as nonradiative recombination centers are annihilated, which are referred to as annealing, may run concurrently with defect multiplication and propagation processes. An extended MCM that is capable of describing annealing in the presence of degradation is presented in this chapter.

Kobayashi and Furukawa[35] were the first to propose a defect model (K-F model) to explain an observed annealing effect in remote junction heterostructure (RJH) lasers. The K-F model postulates that the change in threshold current is proportional to the population of nonradiative recombination defects, and that these nonradiative recombination defects migrate to the p-n junction, when the diode is forward biased, and annihilate there. Since the defects are removed by the bias current, the threshold current is consequently reduced upon aging. Fatt[36] used an extended defect model[37] (EDM), an extended version of the K-F model, to explain the observed annealing effect in double-heterostructure laser diodes. Similar to the K-F model, Fatt attributed the improvement of I_{th} to the reduction of nonradiative recombination centers.

In this chapter, the extended MCM is compared to aging data that were obtained from a set of high-power lasers. In chapter 2, 2-kh aging data for 1310 nm DFB lasers that exhibited wearout degradation in the aging curves was presented.[34] These DFB lasers exhibited weak annealing in the first 44 to 100 hours, as evidenced by the ratio of the annealing to the overall degradation. The length of annealing period (< 100 hours) was negligible on the scale of 2 kh, and the magnitude of annealing (~ 0.5 mA) was relatively small compared to the magnitude of degradation (≥ 10 mA). The aging data that is presented in this chapter, which are for a different type of laser and different aging conditions than reported in chapter 2, exhibit observable annealing over 1000 hours with a magnitude of annealing that is comparable to or greater than the magnitude of the degradation. Since this longer annealing period in the new aging data covers a greater time span, it affects the fitting quality of the MCM and thus annealing must be included. In this chapter, an extended MCM to include annealing and a comparison between the extended MCM and the EDM (an existing defect annealing model) are presented.

3.2 EXPERIMENTAL PROCEDURE

The aging experiments involved biasing a set of 1310 nm multi-quantum-well Fabry-Perot (MQW FP) InGaAsP/InP lasers with 400 mA current under 100 ºC for 5290 hours. The output power and voltage (L-I-V) of the lasers were

periodically measured in an *ex-situ* station at room temperature (25 °C). Ten lasers were selected from a group of aged lasers for this study based on the criterion that they all exhibited pronounced degradation in I_{th}.

3.3 THEORY

To model the aging of a semiconductor laser, I assume, as suggested by Chuang *et al.* [3], that the change in threshold current with time, $\Delta I_{th}(t)$, is caused by the change over time in the nonradiative recombination current. In this extended MCM, I introduce a quadratic term in n_{th} to account for the observable effect of annealing. The change in threshold, ΔI_{th}, in the extended MCM is written as

$$\begin{aligned} \Delta I_{th}(t) &= I_{th}(t) - I_{th}(0) \\ &= I_{nr}(t) - I_{nr}(0) + B\left[n_{th}^2(t) - n_{th}^2(0)\right] \end{aligned} \tag{3.1}$$

where B is a power-series expansion coefficient and $I_{nr}(t)$ is given by Eq. (2.2). Equation (3.1) is an approximation for the change in threshold. Since not all nonradiative recombination processes are included explicitly, the term $B[n_{th}^2(t) - n_{th}^2(0)]$ represents the collective annealing effect in Auger, surface, leakage, and amplified spontaneous emission. In principle, with knowledge of all the recombination coefficients, one could modify Eq. (3.1) to include all the recombination processes and presumably obtain a more accurate fit to the aging data. However, one does not have the knowledge of all the coefficients, and thus

the minimum number of terms is used to describe the annealing and the degradation effects as shown Eq. (3.1). Alternatively, one can interpret the terms $I_{nr}(t) - I_{nr}(0)$ and $B[n_{th}^2(t) - n_{th}^2(0)]$ to be the linear and quadratic terms of a power series expansion of ΔI_{th} in n_{th}. Then, Eq. (3.1) is the second-order power series approximation for the change in threshold in n_{th}.

In chapter 2, it was assumed that I_{nr} could only be affected by the change in N_d.[34] To account for defect annealing, another factor that can modify I_{nr} and I_{th} directly during aging is incorporated. This annealing factor is related to the rate at which defect annealing progresses and is analogous to a reverse process of saturable defect generation. Among the variables that I_{nr} depends on, q and V are constant during aging, and it is assumed that A and η_i are also constant over time. Consequently, there are only two ways that I_{nr}, and thus the threshold current, can be changed during aging. The first way is through changes in the density of nonradiative recombination centers N_d, and the second way is through changes in the threshold carrier density, n_{th}.

The threshold carrier density n_{th} is related to the internal loss in the waveguide of the laser, α_i, and the mirror loss, α_m[38], through

$$\Gamma g_0 \ln\left(\frac{n_{th}}{n_{tr}}\right) = \alpha_i + \alpha_m, \tag{3.2}$$

where Γ is the optical confinement factor, g_0 is a gain coefficient, n_{tr} is the carrier density at transparency, and the logarithmic dependence is a form typically assumed for quantum well devices[39]. The internal loss is associated with the

attenuation of the laser light over a distance L in the cavity, which is described in the form of $\exp(-\alpha_i L)$ where the loss per unit length is defined as the internal loss α_i. The internal loss is generally associated with optical defects that scatter and absorb quanta of light in the laser cavity. Please note that α_i is associated with optical defects as opposed to nonradiative recombination centers or defects, since internal loss affects the output intensity, slope efficiency, and threshold carrier density, but nonradiative recombination centers only directly affect the threshold current.

All the observable defect annealing is arbitrarily assigned to $\alpha_i(t)$. To keep the theory general, the defect annealing is treated such that it does not merely include the annealing of optical defects, but could also include other mechanisms that change the internal loss. For instance, the p-contact resistance in the Ti/Pt/Au system has been observed to decrease after aging in the lasers used in a previous study[34] and after thermal annealing[40,41]. The reduction of contact resistance then decreases the joule heating and improves the internal loss since $\alpha_i = \alpha_i(T)$.[42] There are at least two ways to describe the annealing effect. The first method takes the form for $\alpha_i(t)$ similar to the annealing current proposed in the K-F model[35]:

$$\alpha_i(t) = \alpha_0 + \alpha_1' \exp(-\psi t), \tag{3.3}$$

where α_0 is the ultimate baseline of the internal loss, $\alpha_0 + \alpha_1'$ gives the initial internal loss, and ψ is a positive rate of reduction of the internal loss and is a function of temperature.

In developing a defect-annealing model, the time evolution of internal loss is constructed as a sum of degradation $\alpha_1(t)$ and annealing $\alpha_2(t)$:

$$\alpha_i = \alpha_0 + \alpha_1(t) + \alpha_2(t) \tag{3.4}$$

where α_0 is a constant offset that will not be modified due to aging. The degradation process $\alpha_1(t)$ is assumed negligible and the annealing process $\alpha_2(t)$ is emphasized. The annealing effect in $\alpha_2(t)$ is analogous to a reverse process of saturable defect generation discussed in chapter 2. The rate equation for $\alpha_2(t)$ can then be written as:

$$\frac{d\alpha_2(t)}{dt} = -\hat{R}L\alpha_{i\max}\alpha_2(t)\left[1 - \frac{\alpha_2(t)}{\alpha_{i\max}}\right]. \tag{3.5}$$

The annealing process is limited by the maximum reducible internal loss given by $\alpha_{i\max}$, and saturates under the rate determined by $\hat{R}$ and $L\alpha_{i\max}$. Then, the expression of $\alpha_i(t)$ for the range between $\alpha_2(t)$ and $\alpha_2(0) = \alpha_{i\max} - \alpha_{init}$, where both $\alpha_{i\max}$ and α_{init} are positive constants with $\alpha_{i\max} > \alpha_{init}$, can be rewritten as (see Sec. 7.1 for the solution to the differential equation in Eq. (3.5)):

$$\alpha_i(t) = \alpha_0 + \alpha_{i\max} - \frac{\alpha_{i\max}\alpha_{init}}{\alpha_{init} + (\alpha_{i\max} - \alpha_{init})\exp(-\hat{R}L\alpha_{i\max}t)}. \tag{3.6}$$

Eq. (3.6) is the major result on defect annealing effect. The rate of saturation $\hat{R}$ in Eq. (3.6) is assumed to be temperature dependent but aging time independent, i.e.,

$$\hat{R} = \hat{R}_0 \exp\left(-\frac{E_{a\alpha}}{kT}\right), \tag{3.7}$$

where $\hat{R}_0$ is the rate of reduction of the internal loss as temperature goes to infinity, k is Boltzmann's constant, and T is the absolute temperature. The thermal activation energy associated with defect annealing is called $E_{a\alpha}$ to distinguish it from other activation energies defined in the original MCM[34] for nonradiative recombination centers. In addition to temperature dependence, the rate of saturation $\hat{R}$ could also depend on the bias current, which makes it one type of recombination enhanced annealing. However, there is no data on the current dependence of the optical defect annealing for the lasers under test. Assuming $\alpha_l(t)$ is negligible, the threshold carrier density is affected by the defect annealing such that

$$n_{th}(t) = n_{tr} \exp\left(\frac{\alpha_0 + \alpha_m}{\Gamma g_0}\right) \times \exp\left[\frac{1}{\Gamma g_0}\left(\alpha_{i\,max} - \frac{\alpha_{i\,max}\alpha_{init}}{\alpha_{init} + (\alpha_{i\,max} - \alpha_{init})\exp(-\hat{R}L\alpha_{i\,max}t)}\right)\right]. \tag{3.8}$$

Only a single-component case for α_i is considered in this case. A treatment of multi-component annealing, analogous to the multi-component defect generation in MCM, is certainly possible.

If a non-interacting-defect model is assumed and that the change in I_{th} is caused by the change in I_{nr} and the change in α_i, then Eq. (3.1) becomes[34]

$$\Delta I_{th}(t) = B\left[n_{th}^2(t) - n_{th}^2(0)\right] + \frac{qVA}{\eta_i}\left[\sum_{m=1}^{\varsigma} \frac{M_{nm} N_{dm}(0) n_{th}(t)}{N_{dm}(0) + (M_{nm} - N_{dm}(0)) \exp[-C_{nm} V M_{nm} t]} - N_{dm}(0) n_{th}(0)\right] \quad (3.9)$$

where the time dependence of n_{th} is given by Eq. (3.8). Eq. (3.9) is the major result of this work. The first term of Eq. (3.9) is the new extension to the original MCM[34], which describes the observable annealing effect through the change in α_i. The second term of Eq. (3.9) is the original MCM for describing the observable degradation in terms of a sigmoidal increase in the defect density, which affects I_{nr} directly during aging. The summation sign in the original MCM term signifies the presence of multiple components or degradation mechanisms in the system, and these degradation components can be interpreted as the growth of nonradiative recombination defect complexes by way of depleting finite resources in the vicinity of the defect complexes. M_{nm} and $N_{dm}(0)$ in the original MCM term mark the maximum density and minimum density of the m-th type of defect existing in the active region respectively, and $C_{nm}N_{dm}(t)$ is the rate of saturation of the defect density of the mth type.

The result of Eq. (3.6) will be referred to as the optical defect (OD) annealing as opposed to the annealing effect proposed in the K-F model and the EDM, which is termed as the nonradiative recombination enhanced (NRE) annealing. In summary, the difference between the OD annealing and the NRE

annealing is that OD annealing occurs in the internal loss α_i where it affects the threshold carrier density and the differential quantum efficiency directly, while the NRE annealing requires bias current to assist the annihilation of the nonradiative recombination defect at the p-n junction. While these two annealing mechanisms may both be affected by heat and bias current level, there is no evidence to suggest that the OD annealing and the NRE annealing are connected or unrelated. In our case, I assume the two annealing mechanisms to be independent processes.

3.4 EXPERIMENTAL RESULTS AND DISCUSSIONS

3.4.1 Fitting results using the degrading MCM and the OD annealing models

Figure 3.1 shows an example of a threshold aging curve fitted by this extended MCM. In fitting all the experimental data, a one-component degrading MCM model (ς=1 in Eq. (3.9)) and the OD annealing model (Eq. (3.8)) were used, and it was assumed no NRE annealing. This assumption will be explained later. Since the information on Γg_0 is not known, Γg_0 = 1 is assumed and the information of Γg_0 is allowed to be embedded in $\alpha_{i\,max}$ and α_{init} during fitting. Please note that although the extended MCM was presented as "multi-component" in a sense that there are two existing mechanisms: the degrading MCM mechanism and the OD annealing mechanism, the result is presented as

"one-component" in the degrading MCM mechanism and the OD annealing mechanism. Through the extended MCM, these two models are then combined into one single model with two mechanisms (degrading MCM and OD annealing) and multi-components in the degrading MCM.

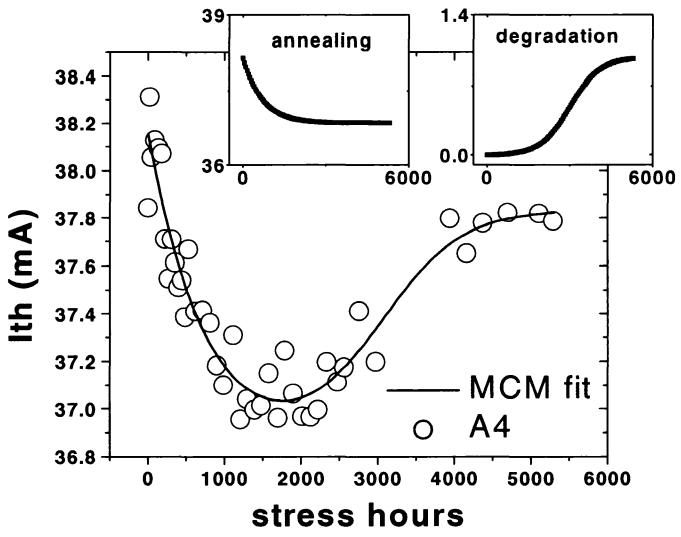

Fig. 3.1. An aging plot of the threshold current of laser A4 and the corresponding fit using a one-component MCM incorporated with annealing effect. The insets show the components of the MCM fit: annealing and degradation with x-axis in hours and y-axis in mA.

The two terms in Eq. (3.9) that constitute the whole threshold aging curve are shown in the insets of Fig. 3.1. The OD annealing component (inset "annealing" of Fig. 3.1) is the first term in Eq. (3.9) and the degradation component (inset "degradation" of Fig. 3.1), which represents ΔI_{nr}, is the second term in Eq. (3.9). The OD annealing component consists of the collective effect

of the annealing-induced change in Auger, surface, leakage, and amplified spontaneous emission, all of which depend on α_i through n_{th}. Although the OD annealing effect in n_{th} also affects I_{nr}, the overall threshold reduction is often masked by the defect-induced degradation. In principle, if degradation owing to defect generation is negligible, then a clear OD annealing effect similar to the "annealing" inset of Fig. 3.1 should be observed. Examples of this type of annealing effect can also be found in work by Asahi *et al.*[43]

Fig. 3.2 shows two more fitting examples (lasers A7 and A3X) using the extended MCM to confirm that the extended MCM provides satisfactory fitting to other aging data as well. The fitting results along with the results of the rest of the 10 lasers are all tabulated in Table 3.1. Due to the lack of space, the uncertainties associated with the fitted parameters are not listed, except for laser A4. However, the uncertainties for each laser are similar to those presented in the column of A4. Please note that the uncertainties quoted in the table are obtained by multiplying the standard deviations from the error matrix with the standard deviation of the fit, $\sqrt{S^2}$. Please also note that the covariances have not been included in Table 3.1.

If Eq. (3.9) is a reasonable description of the physical reality, then the observable defect annealing must occur by the route of modifying the internal and/or mirror loss as suggested by Eq. (3.8). Additional experimental evidence that defect annealing is observable by the change in internal loss is the time dependent behaviour of the slope efficiency, which is proportional to the

differential quantum efficiency. The expression for the differential quantum efficiency, η_d, is given as[38]

$$\eta_d = \eta_i \frac{\alpha_m}{\alpha_i + \alpha_m}. \tag{3.10}$$

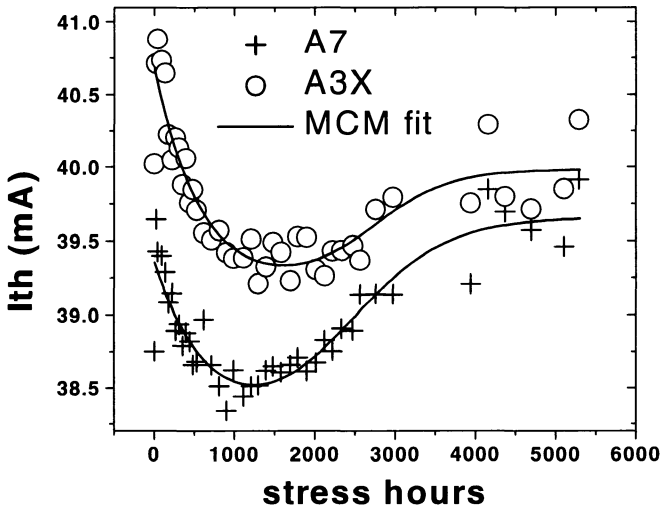

Fig. 3.2. Examples of the MCM fits performed on two other threshold aging curves.

The differential quantum efficiency η_d is a function of the internal loss α_i, the mirror loss α_m, and the injection efficiency η_i, but does not directly depend on N_d. So if there is any change in α_i (or α_m) as suggested in Eq. (3.3), the annealing effect should be readily observed in the differential quantum efficiency. On the other hand, if only N_d changes, the observable annealing effect should be minimal due to an indirect influence on η_d, provided η_i is not a function of N_d.

Samples	A4	A5	A6	A7	A8	A2X	A3X	A4X	A5X	A6X
$B\, n_{tr}^2 \exp\left[2\left(\frac{\alpha_0+\alpha_m}{\Gamma g_0}\right)\right]$ (mA)	36.9 ± 0.7	36.3	36.6	38.1	36.3	38.4	39.2	38.7	38.4	37.1
Scaled $\alpha_{imax}/(\Gamma g_0)$	0.12 ± 0.04	0.15	0.12	0.13	0.15	0.13	0.16	0.17	0.20	0.21
Scaled α_{init} (cm^{-1})	0.10 ± 0.06	0.13	0.11	0.11	0.13	0.11	0.14	0.15	0.18	0.19
$\hat{R}L$ (cm-hour^{-1} $\times 10^{-4}$)	131 ± 99	84	155	123	70	85	125	77	66	84
$\frac{qV}{\eta_i} A\, n_{tr} \exp\left(\frac{\alpha_0+\alpha_m}{\Gamma g_0}\right)$ (mA-cm^3)	0.02 ± 0.05	0.04	0.95	0.29	0.04	0.05	0.03	0.16	0.18	0.02
Scaled $C_{nl}V$ (10^{-4} cm^3-hour^{-1})	0.40 ± 0.79	0.87	5.18	3.13	1.06	1.20	0.72	1.76	2.08	0.49
Scaled M_{nl} (cm^{-3})	46 ± 80	28	2	5	19	20	29	10	8	66
Scaled $N_{dl}(0)$ (cm^{-3})	0.16 ± 0.74	0.09	0.10	0.10	0.20	0.10	0.10	0.10	0.10	0.11
Variance of fit, S^2	0.017	0.034	0.029	0.033	0.035	0.051	0.041	0.058	0.043	0.139

Table 3.1. The fitted parameters of the MCM to 10 MQW FP lasers assuming $\Gamma g_0 = 1$.

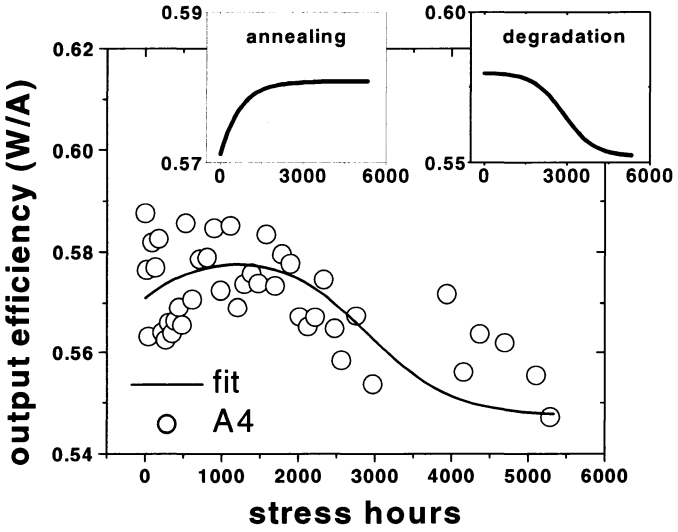

Fig. 3.3. The output efficiency of laser A4 at operating current. The insets show the components of the fit: annealing and degradation with x-axis in hours and y-axis in mA.

Evidence that the slope efficiency increases as a function of time due to the OD annealing is presented in Fig. 3.3. The components of the fitted curve (annealing and degradation) are presented in the insets. In a preliminary study of the slope efficiency, it was found that the degradation $\alpha_1(t)$ (see degradation inset) is mainly caused by the temperature increase that is accompanied with higher threshold current and the annealing (see annealing inset) is described in Eq. (3.6). This suggests that $\alpha_1(t) \neq$ constant and may not be negligible as was suggested earlier. However, $\alpha_1(t)$ pairs with the nonradiative-recombination-enhanced degradation as a response of the system to a temperature change due to

degradation. Therefore, the effect of $\alpha_1(t)$ is embedded in the coefficients of the MCM, which effectively allows to neglect $\alpha_1(t)$ in the extended MCM. The fitted curve in Fig. 3.3 displays a peak between 1000 and 1500 hours which results from the superposition of the annealing and degradation components. This observation supports the idea that the observable annealing effect is more likely caused by an improvement in the internal loss, rather than by the reduction of the density of nonradiative recombination centers. However, the mathematical framework of the extended MCM can include both OD annealing and NRE annealing if necessary. In principle, there could have been changes in α_m. The observable effect of changes in α_m would be a change in the slope efficiencies of the output for each facet. Measurements do not exist for both facets and thus α_m is treated as a constant in our case and all changes are arbitrarily ascribed to α_i.

As mentioned earlier, the aging data presented in chapter 2 exhibit weak annealing, and can be fitted by the extended MCM for this reason. A plot of I_{th}-aging time data fitted by the extended MCM is presented in Fig. 3.4. It is found that the χ^2 has been reduced to 0.017 using the extended MCM, in comparison to 0.022 obtained from fitting with the MCM which neglects the annealing effect. To test for significance[44] (see chapter 2 for the test method), $f = 0.022/0.017 = 1.29$ which is smaller than the critical value 2.50 for a confidence level of 99%. In other words, the improvement in the fit quality using the extended MCM is not statistically significant. Thus, it justifies that it was legitimate to neglect the annealing effect in the aging data represented in chapter 2 as was assumed.

However, it is clear that the short annealing effect in the early aging stage is accounted for using the extended MCM (see the inset in Fig. 3.4).

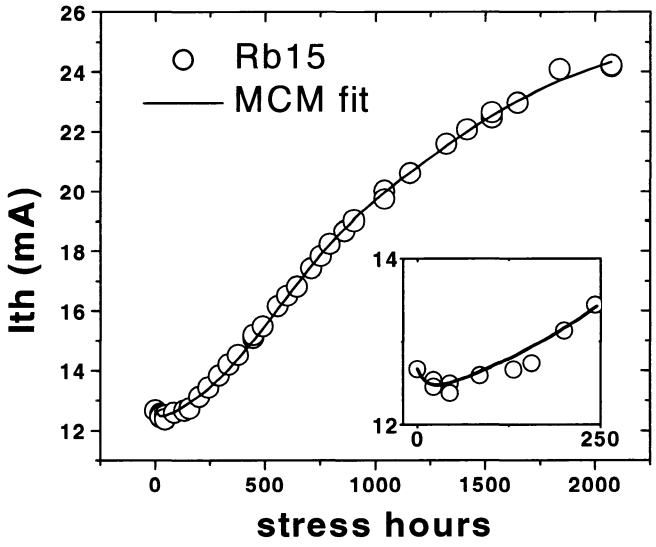

Fig. 3.4. Fit of aging data from Ref. 34 using the extended MCM fit. The inset zooms in the short annealing period in the aging data.

3.4.2 Comparison with the EDM

In this section, a comparison between the extended MCM and the EDM[36,37] is presented. The EDM is defined as,

$$\begin{aligned} \Delta I_{th} &= I_{th}(t) - I_{th}(0) \\ &= I_{th1}t + I_{th2}[1 - \exp(-k_1 t)] + I_{th3}[1 - \exp(-k_2 t)] \end{aligned} \tag{3.11}$$

where

$$
\begin{aligned}
\mathrm{I}_{\mathrm{th1}} &= I_{th}^{0}\gamma\tau_{s}^{0}\beta I^{n} \\
\mathrm{I}_{\mathrm{th2}} &= I_{th}^{0}\gamma'\tau_{s}^{0}N_{0}{}'\left(\frac{d'}{d}\right) \\
\mathrm{I}_{\mathrm{th3}} &= I_{th}^{0}(\gamma'-\gamma)\tau_{s}^{0}\left(N_{0}-\frac{\beta}{\alpha}I^{n-m}\right) \\
\mathrm{k}_{1} &= \kappa I^{p} \\
\mathrm{k}_{2} &= \alpha I^{m}
\end{aligned}
\tag{3.12}
$$

in Horikoshi's notations[37], and the meaning of the variables can be found in this work. I simplified the coefficients into five constant variables as shown in Eq. (3.12). The interpretation of Eq. (3.11) is as follows: the first term is the linear long-term degradation, the second term is the saturable degradation term that provides similar saturable effect in the MCM, and the third term is the annealing term.

Figure 3.5 shows the aging data in Fig. 3.1 fitted by the EDM. In fitting laser A4, the linear degradation coefficient, I_{th1}, is assumed to be zero, since a linear degradation is not observed. The corresponding fit coefficients are tabulated in Table 3.2. Since the variances of the fits by MCM and by EDM are the same statistically, the qualities of the fits are basically the same. Therefore, the fit provided by the MCM is not significantly better than the fit provided by the EDM. When comparing the inset diagrams in Fig. 3.1 and Fig. 3.5, it is found that the estimated overall annealing (5.47 mA) and overall degradation (5.22 mA) components for EDM are much larger than that for the MCM (overall annealing = 1.30 mA; overall degradation = 0.97 mA), due to the nature of the model. EDM is comprised of exponential functions as opposed to MCM, which is comprised of

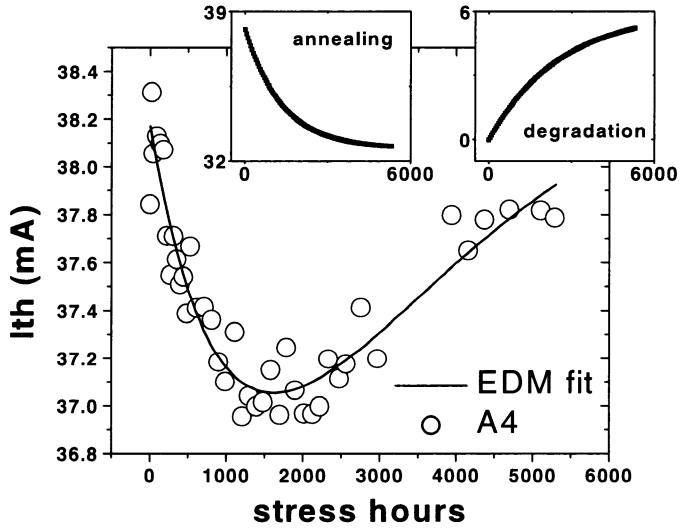

Fig. 3.5. An aging plot of the threshold current of laser A4 and the corresponding fit using EDM. The inset shows the components of the EDM fit: annealing and degradation with x-axis in hours and y-axis in mA.

sigmoidal functions. Since the annealing and degradation are two competing exponential curves in the case of EDM, the EDM generally requires a relatively large magnitude in annealing and degradation to create the observed valley. Due to this reason, the uncertainties associated with the EDM fit are larger compared to the MCM as the valley becomes prominent (see Table 3.2). On the other hand, the formation of a valley is quite natural by shifting the annealing and degradation curves in the time domain for the MCM. Basically, when the annealing is strong and the degradation curve is in the early stage of the sigmoidal curve, a valley forms. Therefore, it appears that the EDM fit overestimates the magnitude of annealing and degradation in these annealed and degraded samples.

EDM	
Fit coefficients	Values
$I_{th}(0)$ (mA)	38.17 ± 0.07
I_{th1} (mA)	0
I_{th2} (mA)	6 ± 43
k_1 (10^{-4} h^{-1})	4 ± 21
I_{th3} (mA)	-6 ± 44
k_2 (10^{-4} h^{-1})	8 ± 7
S^2	0.017

Table 3.2. The fitted parameters of EDM corresponding to the results in Fig. 3.5.

3.4.3 Nonradiative recombination enhanced defect annealing

The reduction of the nonradiative recombination[35,36,37,45,46,47], N_d, and the reduction of internal loss in the waveguide of the laser[48,49], α_i, under accelerated aging are both considered as defect annealing. To my knowledge, defect annealing is not as of yet an entirely understood phenomenon. I believe that both defect annihilation (nonradiative recombination enhanced annealing) and internal loss reduction (optical defect annealing) occur during defect annealing, but I cannot provide rigorous proof that these mechanisms are independent as I have assumed. However, I believe that only the effect of internal loss reduction (α_i and/or α_m) can be observed in our aging curves in this particular study, because

NRE defect annihilation cannot directly improve slope efficiency in such a large scale that is evident in Fig. 3.3.

The evidence presented in the samples, however, cannot erase the possibility of defect annihilation being observed in other laser samples. Thus, the effect of NRE annealing in the MCM will be explored in this section. First, introduce an $\alpha I^m N_d(t)$ term for defect annihilation in the MCM defect density rate equation, as explained in Refs. 35, 36, and 37. While it may be argued that the expression describing defect annihilation should be proportional to the carrier density product np or n^2 for $n \cong p$ in the active region to represent the recombination-driven nature of the NRE annealing, this carrier density product form is not important in the present case, because the aging current is set as a constant variable throughout the experiments. It will be assumed the NRE defect annihilation takes the form of $\alpha I^m N_d(t)$. If the defect annihilation and defect generation are two coupled mechanisms (i.e., they share the same defect population[35,36,37]), then the rate equation for describing the defect dynamics[34] becomes

$$\frac{dN_d(t)}{dt} = N_d(t)\left[K_n + C_n - \alpha I^m\right] - C_n V N_d^2(t). \qquad (3.13)$$

where N_d is the defect density for one particular type of defect, and $K_n + C_n$, αI^m, and $C_n V N_d(t)$ are the rate of growth, the rate of defect annihilation, and the rate of saturation of the defect density respectively. The first term in Eq. (3.13) gives the rate of growth of the defect density, and the second term is a limiting factor that

drives the rate of change of N_d to saturate with time as the raw materials required for growth of defects are consumed. Please note that if $K_n = C_n = 0$, then Eq. (3.13) will produce the form of $N_d(t)$ proportional to $\exp(-\alpha I^m t)$ which coincides to the form of defect annealing or annihilation utilized in the K-F model[35] and EDM[36,37]. Since the bias current I is constant and equal to the aging current which is 400 mA for the experiments, the solution of Eq. (3.13) is

$$N_d(t) = \frac{M_n N_d(0)}{N_d(0) + (M_n - N_d(0))\exp[-C_n V M_n t]} \tag{3.14}$$

where

$$M_n = \frac{K_n + C_n - \alpha I^m}{C_n V},$$

$$K_n = \kappa n^2 \exp\left(-\frac{E_a}{kT}\right), \tag{3.15}$$

and

$$C_n = cn^2 \exp\left(-\frac{E_a}{kT}\right).$$

The form of N_d is identical to what I proposed in chapter 2, except M_n is now offset by a constant value, $\alpha I^m/(C_n V)$. This argument suggests that the defect annihilation, described by αI^m, may be present but cannot be separated from other aging effects if $\alpha I^m < (K_n + C_n)$, according to Eqs. (3.14) and (3.15). However, one would be able to observe the NRE annealing effect due to defect annihilation if $\alpha I^m > (K_n + C_n)$. Then, the rate of the NRE annealing would depend on the

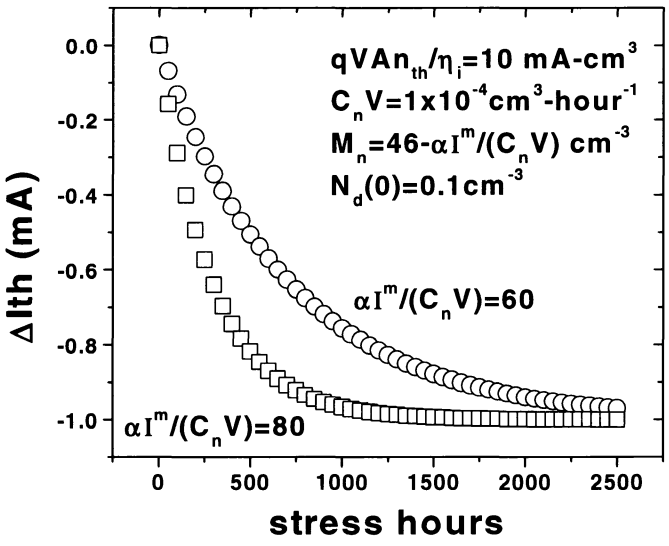

Fig. 3.6. Plot of ΔI_{th} as a function of aging time for the cases: $\alpha I^m/(C_n V) = 60$ and 80 cm^{-3}, where $\alpha I^m > (K_n + C_n)$ with $(K_n + C_n)/(C_n V) = 46$.

aging current level as depicted in Fig. 3.6. This result coincides with the annealing results as reported by Kobayashi and Furukawa[35]. The important characteristic of this proposed NRE annealing is that the threshold current only decays but cannot rebound to form a valley, assuming both defect generation and annihilation occur and saturate simultaneously. Since a rebound on I_{th} is observed in the samples (see Fig. 3.1), this implies that the observed effect is caused by the OD annealing or reduction of internal loss rather than the NRE annealing.

A second scenario, where the defect generation and annihilation are two independent processes, could occur and allow observation of the NRE annealing. I propose that independent NRE annealing should have a sigmoidal form, based

on the argument that I used to derive Eq. (3.6). Then the extended MCM with NRE annealing can be written as,

$$\Delta I_{th}(t) = \frac{qVAn_{th}}{\eta_i}\left[\frac{M_n N_d(0)}{N_d(0)+(M_n - N_d(0))\exp[-C_n V M_n t]} - N_d(0)\right] + \frac{qVAn_{th}}{\eta_i}\left[-\frac{M_n^{anneal} N_d^{anneal}}{N_d^{anneal}+(M_n^{anneal} - N_d^{anneal})\exp[-C_n^{anneal} V M_n^{anneal} t]} + N_d^{anneal}\right]. \quad (3.16)$$

In this case, the maximum annealing is limited by M_n^{anneal} which is a characteristic constant, N_d^{anneal} is a constant which is less than M_n^{anneal}, and C_n^{anneal} is a rate constant that has a temperature dependence based on a Boltzmann factor. n_{th} is assumed to be pinned. Extended from this second scenario, a laser sample could have both NRE and OD annealing coexisting, in a case in which the NRE annealing is independent of defect generation. Each mechanism, in this case, can be treated as an independent module based on Eqs. (3.8) and (3.16).

3.4.4 Annealing-degradation interactions predicted by the extended MCM

Using the extended MCM, it is possible to show that the annealing and degradation are two competing mechanisms (see Fig. 3.1). I believe that defect annealing is apparent in the threshold aging data, because in the early stage of the sigmoidal curve, the degradation is relatively insignificant or is generally weak (reliable lasers with low degradation). Alternatively, if the NRE defect annihilation dominates the NRE defect generation, then the NRE annealing is

observed. On the other hand, if degradation is severe, then defect annealing will be masked. Four aging curves corresponding to different level of annealing defined by α_{imax}, which measures the maximum change of the internal loss or the level of OD annealing, are plotted in Fig. 3.7. The degradation component is plotted according to a two-component MCM with the coefficients based on one of the lasers presented in chapter 2 and the annealing component based on measurements obtained in this chapter. The purpose of Fig. 3.7 is to demonstrate that the shape of the aging curve can take on different characteristics depending on the ratio between the OD annealing and degradation components. In Fig. 3.7, the threshold current is just a simple two-component degradation case in the case of zero annealing ($\alpha_{imax} = 0$) as shown in chapter 2. When α_{imax} increases to 0.34, the threshold aging curve starts to resemble the curves presented in Fig. 5 of Ref. 36 which exhibits a peak on the I_{th}-aging time curve. Please note that the value assigned to α_{imax} is a scaled value rather than an absolute physical value. As α_{imax} increases to 0.60, I notice that the annealing creates a small valley in the first 400 hours of the aging curve as shown in the inset of Fig. 3.7. In reality, this type of short-term small valley or negative degradation (ΔI_{th} is negative) in the threshold aging curve (see the inset of Fig. 3.4) is observed. This small valley signifies the presence of the annealing component being masked by the degradation component. Depending on the time constant for the annealing component, one may see a decrease in the threshold current following a peak as

shown in the case of $\alpha_{imax} = 0.34$ and 0.60. The presence of the small valley occurring in the early aging also provides important evidence that an

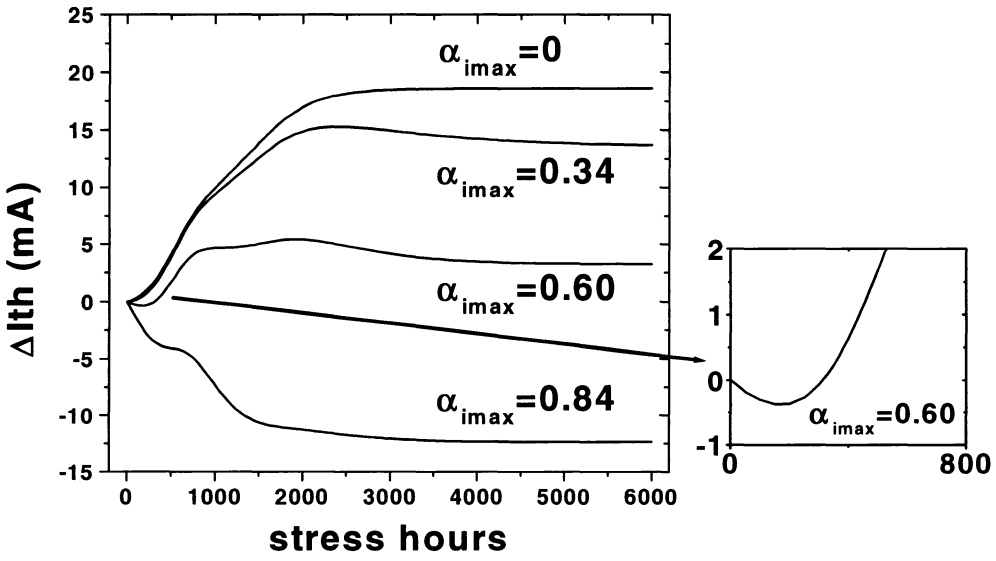

Fig. 3.7. Simulated results using a two-component MCM with various levels of annealing measured by the scaled α_{imax}. The inset zooms in the early degradation of the annealed curve, where $\alpha_{imax} = 0.60$, to show the negative degradation in the first 500 hours.

appropriate aging model should take the form of a sigmoidal curve rather than the exponential type used in EDM. As discussed earlier, the sigmoidal curve tends to have a flatter region in the early aging, so even a weak annealing could be detected as a small valley. However, if an exponential curve were employed in this case, it would take a strong annealing to overcome the rapid initial increase in an exponential curve in order to form a small valley.

The interesting part of using a two-component MCM for degradation can be shown in the strongly annealed case ($\alpha_{imax} = 0.84$) in Fig. 3.7. The aging curve exhibits steps between 0 and 2000 hours. The two steps in the aging curve signify the presence of the two-component degradation, which is partially masked by the annealing component. Among the lasers that were studied in this work, laser A5 exhibits step-like annealing similar to the strongly annealed case in Fig. 3.7. To enhance the viewing of the steps in laser A5, a 3-point smoothing on the aging data was performed and the result is plotted in Fig. 3.8. One can observe in Fig. 3.8 that a pronounced step occurs at around 400 hours and an unpronounced step occurs at around 900 hours.

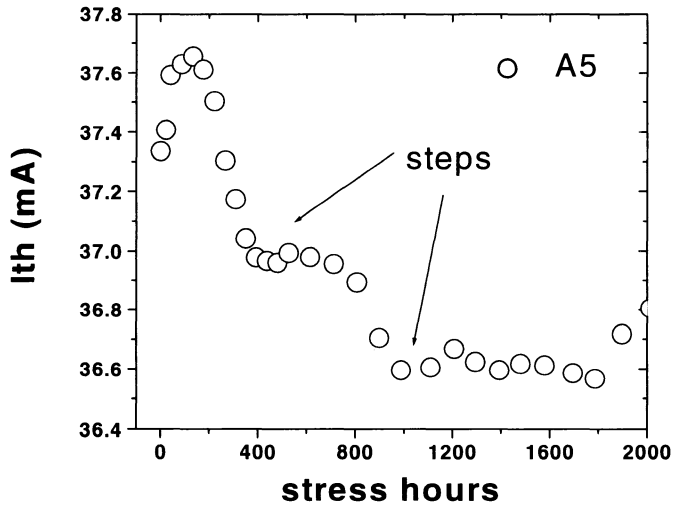

Fig. 3.8. Example of a MQW FP laser (labeled as A5) that exhibits steps in the annealing component.

3.5 CONCLUSION

An extended version of the MCM is presented in this chapter. It is shown that using this approach, it is possible to fit to the experimental device aging data, and to describe saturable threshold current and defect annealing. The model is able to account for some subtle details such as the peak observed in the I_{th}-time curve as the degradation saturates, the short-term small valley (negative degradation) occurring in the I_{th}-time curve in the early aging, and steps occurring in the annealing component. It was proposed that the observed defect annealing is caused by the improvement in the internal loss during aging, which was termed the optical defect annealing.

Without contradicting the EDM, the extended MCM describes nonradiative recombination enhanced defect annihilation during aging. However, the optical defect annealing case was used, because it explains the annealing effect occurring in the slope efficiency in the samples studied. In the case when NRE annealing is coupled with defect generation, it was shown that NRE defect annihilation is masked by defect generation and can only be observed if the NRE defect annihilation term αI^m is larger than the defect generation term $K_n + C_n$. Also, the possible scenario when NRE defect annihilation is independent of the defect generation was discussed, and the corresponding new form of MCM incorporating this type of NRE annealing was derived. In comparison with the EDM, It is concluded that the extended MCM provides fits to the experimental

data with comparable quality. However, I believe that the extended MCM provides more reasonable results than those estimated by the EDM.

CHAPTER 4. EFFECTS OF HAVING TWO POPULATIONS OF DEFECTS GROWING IN THE CAVITY OF A SEMICONDUCTOR LASER

4.1 INTRODUCTION

Attempts to model early aging data to predict long-term aging behaviour have been made in the past[2,3,4,30], but none of these models, in my opinion, provides a satisfactory explanation to the long-term aging behaviour of semiconductor lasers. To simplify the problem, some models suggest that the long-term degradation progression varies in a linear fashion over time[4,30]. The lifetime of a device, under this assumption, can then be estimated linearly after bypassing the transient low-activation-energy modes or burn-in period.[2,4,50,51] Alternatively, Kondo *et al.*[15] proposed that the long-term degradation should be described by a cosh function or an exponential function of aging time. Many attempts to describe the aging of devices are device-specific, or failure-mode specific, and do not provide an organized, broader explanation to the generic degradation behaviour. The MCM provides a much broader theory to explain the degradation of threshold in general. In this chapter, the MCM is used to explain why a universal aging curve is seldom presented. Insight to the estimation of the activation energy and the device lifetime is presented. Through the inspection of several case studies, it is shown that the MCM does indeed provide a general analytical model for the aging of semiconductor lasers.

4.2 THE AGING MODEL

The aging model that is proposed in Eq. (2.11), termed MCM[34], describes the change of threshold current with aging time as ς observed sigmoidal components. Each sigmoidal component is characterized by a corresponding activation energy, which allows each component to be thermally activated to a different degree. The thermally-activated behaviour of a one-component MCM is illustrated in Fig. 4.1, where the aging curve saturates faster at higher temperature relative to the case of lower temperature. The incubation period shown in Fig. 4.1 is defined as the length of time that starts from the initial time to slightly above the inflection point of the sigmoidal curve and below the saturation point. In general, a one-component sigmoidal aging curve has only one incubation period. However, it is shown in Fig. 4.2 that two incubation periods can be observed in a two-component case. Furthermore, the long-term degradation is, in the MCM, another sigmoidal component characterized by a low rate of degradation[34] or often characterized by a high thermal activation energy. The idea that the long-term degradation has a large thermal activation energy has been proposed by Gordon *et al.*[50] and Nash *et al.*[52]

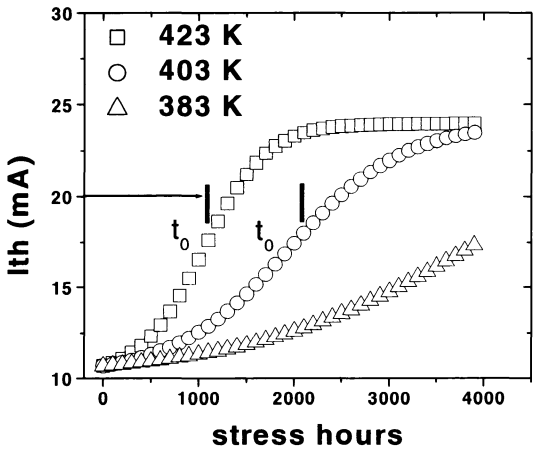

Fig. 4.1. Plots of a one-component MCM with $E_a = 0.45$ eV at three different absolute temperatures: 383, 403, and 423 K. The t_0's mark the incubation periods for each curve. The incubation period for the curve of 383 K is out of bounds.

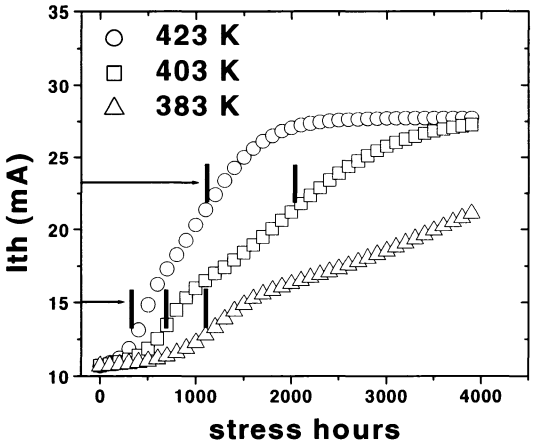

Fig. 4.2. Plots of a two-component MCM with $E_a = 0.35$ and 0.45 eV respectively at three different absolute temperatures: 383, 403, and 423 K. Two incubation periods are involved in this case at approximately the levels of 15 and 23 mA. The second incubation period for the curve of 383 K is out of bounds.

4.3 RESULTS AND DISCUSSIONS

The data that are studied in this chapter are from the set of ridge-waveguide strained multi-quantum-well gain-coupled distributed feedback (RWG MQW GC DFB) lasers recorded in chapter 2.

Hakki *et al.* [4] has proposed a successful empirical model to describe saturable threshold current, and the model, which I call the HFE model, incorporates an activation energy associated with the growth or diffusion of nonradiative centers. The change in threshold as a function of time for the HFE model is,

$$\Delta I_{th}^{HFE}(t) = R_{HFE}t + S\left[\frac{1}{1+\exp[-(t-t_0)/\tau]} - \frac{1}{1+\exp[t_0/\tau]}\right] \tag{4.1}$$

where

$$R_{HFE} = R_{HFE0}\exp\left(-\frac{E_a}{kT}\right). \tag{4.2}$$

R_{HFE} is a constant rate of increase of the long-term degradation, S is the relative strength of the saturable current, t_0 marks the end of the incubation period which is normally omitted in the fitting of aging data to the HFE model, and $1/\tau$ gives the rate of change of the saturable current. The HFE model happens to be a special case of the MCM. If one ignores the "$R_{HFE}t$" term and the incubation period (i.e. set $t_0 = 0$) in Eq. (4.1), and makes the following substitutions in Eq. (2.11): $\varsigma = 1$, $C_{nm} = 1/(2\tau)$, $M_{nm} = 2$, $N_{dm}(0) = 1$, and $qVAn_{th}/\eta_i = S/2$, then Eq.

(2.11) becomes identical to Eq. (4.1). In my opinion, the "$R_{HFE}t$" term for describing the long-term aging behaviour is not physical for a finite system, because it represents a non-saturable aging in the threshold current and requires a constant and therefore infinite supply of resources for growth of the defects. As mentioned before, the long-term degradation is represented as the last component in the MCM, which has a relatively lower rate of degradation. This implies that the long-term degradation will eventually saturate if a long enough aging time is permitted. This consequence agrees with the basic principles of population growth with finite resources.

In addition to the one-component aging curve shown in Fig. 4.1, a two-component aging curve representing devices aged at different temperatures is constructed in Fig. 4.2, using a set of fit coefficients recorded in Table 4.1. The fit coefficients, in Table 4.1, were obtained from fitting the MCM to the experimental data of laser Rb13 by assuming the first and second components to have thermal activation energies of 0.35 and 0.45 eV, respectively. I chose 0.35 and 0.45 eV, because these values are close to values that are reported by Nash *et al.*[52] (0.25 to 0.4 eV for infant failure and 0.5 to 1.5 eV for wearout failure), and the difference between 0.35 and 0.45 eV is large enough to demonstrate clearly the effect I would like to present.

Fit coefficients	Values
I_{th0} (mA)	10.18 ± 0.35
Scaled $\frac{qV}{\eta_i} A n_{th}$ (mA-cm^3)	0.93 ± 0.21
Scaled $cn_{th}^2 V$ (cm^3-hour^{-1})	47.86 ± 16.90
E_{a1} (eV)	0.35
Scaled M_{n1} (cm^{-3})	4.08 ± 1.90
Scaled $N_{d1}(0)$ (cm^{-3})	0.01 ± 0.02
E_{a2} (eV)	0.45
Scaled M_{n2} (cm^{-3})	14.81 ± 2.34
Scaled $N_{d2}(0)$ (cm^{-3})	0.55 ± 0.33
Variance of fit, S^2	0.13

Table 4.1. The fit coefficients of Rb13 using the two-component MCM at 423 K.

Comparing to Fig. 4.1 where the one-component curve retains similar shapes at different temperature levels, the apparent aging behaviour of the two-component MCM in Fig. 4.2 behaves differently at different temperature levels. At 383 K, the behaviour of the two-component MCM is similar to the aging curve presented in Figs. 2 and 3 of Ref. 30 and Fig. 3 of Ref. 4, where there are an exponential-degradation period (also known as the incubation period), followed by a knee (saturation), and a linear long-term degradation. However, when the aging temperature is raised to 403 K, the presence of a single incubation period assumed by Hakki *et al.* [4] is no longer valid, and instead, a second incubation period becomes visible in the time window. Any further increase in the

temperature causes the two components to merge and the incubation periods to recede towards the initial time. The temperature increase at which these incubation periods appear to merge is, of course, related to the relative activation energies for each of the degradation components. The apparent double-sigmoidal shape is transformed into a curve that resembles an exponential function as shown by the curve at 423 K. If the MCM were not available, it would be more reasonable to model the curve at 423 K by the Sim model[2] than by a combination of sigmoidal/exponential curve and a linear curve in the HFE model[4] and the EDM[30].

If the aging time is long enough to reveal all possible components associated with the aging curve, such ambiguity mentioned above should not arise. To demonstrate the importance of the time window over which the degradation is characterized, in affecting perception of the aging curve, plots that illustrate the change in I_{th} (in natural logarithmic scale) with temperature in two time windows (500 to 1000 hours and 1000 to 1500 hours) for one-component and two-component MCM are presented in Fig. 4.3(a) and (b), respectively. The curves follow the the MCM model:

$$\ln[\Delta I_{th}(t_2) - \Delta I_{th}(t_1)] = \ln\left(\frac{qVAn_{th}}{\eta_i}\right) + \ln\left[\sum_{m=1}^{\varsigma} \frac{M_{nm}N_{dm}(0)}{N_{dm}(0) + (M_{nm} - N_{dm}(0))\exp[-cn_{th}^2 \exp(-E_{am}/(kT))VM_{nm}t_2]} - \frac{M_{nm}N_{dm}(0)}{N_{dm}(0) + (M_{nm} - N_{dm}(0))\exp[-cn_{th}^2 \exp(-E_{am}/(kT))VM_{nm}t_1]}\right] \quad (4.3)$$

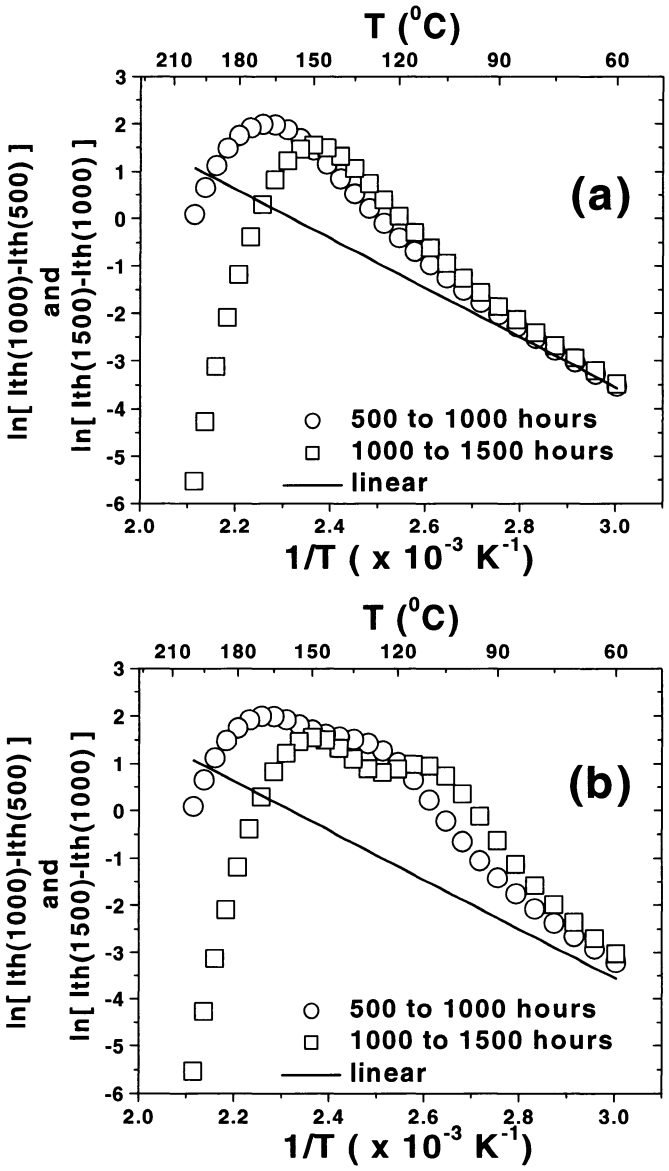

Fig. 4.3. Plots of the difference of I_{th} for (a) one-component MCM with E_a = 0.45 eV and (b) two-component MCM with E_{a1} = 0.35 eV and E_{a2} = 0.45 eV between 500 and 1000 hours and between 1000 and 1500 hours as a function of the inverse of the aging temperature. The solid line is a linear evaluation of I_{th} between 500 and 1000 hours (or 1000 and 1500 hours) as function of temperature.

which can be derived from Eq. (2.11). The coefficients for the two-component case are available in Table 4.1; but for the one-component case, only the coefficients for the second component are used. The y-axis on both Fig. 4.3(a) and (b) is $y = I_{th}(t = 1000 \text{ hours}) - I_{th}(t = 500 \text{ hours})$ and $y = I_{th}(t = 1500 \text{ hours}) - I_{th}(t = 1000 \text{ hours})$ in a logarithmic scale, i.e., the change of threshold current in two time windows. For comparison purpose, I construct a curve based on the assumption of a linear long-term degradation utilized in Refs. 4 and 30. The curve is defined as

$$\ln[\Delta I_{th}(t_2) - \Delta I_{th}(t_1)] = \ln[R_{HFE}(t_2 - t_1)] - \frac{E_a}{k}\left(\frac{1}{T}\right). \tag{4.4}$$

The linear degradation curve in Eq. (4.4) is also plotted in Fig. 4.3(a) and (b), with $R_{HFE} = 362.75 \text{ h}^{-1}$, $E_a = 0.45$ eV, and $t_2 - t_1 = 500$ h. The value of R_{HFE} is chosen such that $R_{HFE} = qV^2An_{th}^3cN_{d1}(0)M_{n1}/\eta_i$ (see Eq. (4.5)). For the one-component MCM, since $cn_{th}^2 \exp(-E_{a1}/(kT))M_{n1}t << 1$ when temperature is low and $M_{n1} >> N_{d1}(0)$, Eq. (4.3) can be simplified to be

$$\ln[\Delta I_{th}(t_2) - \Delta I_{th}(t_1)] \approx \ln\left[\frac{qV^2An_{th}^3c(t_2 - t_1)N_{d1}(0)M_{n1}}{\eta_1}\right] - \frac{E_{a1}}{k}\left(\frac{1}{T}\right). \tag{4.5}$$

Eq. (4.5) explains why the one-component MCM curves in both time windows merge into the linear degradation curve at low temperature in Fig. 4.3(a). The fact that the curves in the two time windows deviate significantly from each other

at high temperature (above 150 °C or below 2.4×10^{-3} K^{-1}) indicates further that the time window during the accelerated aging experiment over which the degradation is characterized is important, especially in high temperature.

For the case of two-component MCM, the behaviour of the curve in Fig. 4.3(b) is very non-linear, time-window dependent, and temperature-range dependent. In the 500-to-1000-hour window, the two-component MCM clearly shows a weak bimodal behaviour (double peak) in comparison to the linear degradation curve (solid line) in Fig. 4.3(b). Unlike the one-component case, the two-component curve in the 1000-to-1500-hour window deviates significantly from the two-component curve in the 500-to-1000-hour window, and the bimodal behaviour becomes more prominent. Furthermore, the change of the two-component curve is most sensitive in the temperature range that most researchers are concerned with for the purpose of accelerated lifetesting, namely, from 100 to 180 °C (or 1/T = 2.21 to 2.68×10^{-3} K^{-1}). The drastic change, which occurs between the two-component curves at different time windows, is caused by the shifting in the partition of the two components. The partition between the two components is defined as the weights of the two components in a time window, and it is affected by the ambient or aging temperature. As a consequence, in some sensitive temperature range (e.g., 100 to 180 °C), it is probable that the analysis of device aging based on a duration of 1000 hours, compared to that of an identical device for 1500 hours would give rise to different conclusions of how I_{th} changes with temperature and different associated activation energies. Therefore, the

reasons why a universal model is seldom presented lie on the ambiguity introduced by: (1) the different levels of stress (e.g. temperature and current) used in the data presented by individual researchers; (2) the neglect of multiple failure modes or defect components; and (3) the different length of aging time presented in the data. Both the one-component and two-component cases start to deviate significantly from the linear degradation curve above 60 °C. This idea suggests that the linear degradation approximation becomes inaccurate at high temperature. Due to the reasons that the MCM seems to consist of a more general form for saturable current and seems to offer a better physical explanation for the long-term aging behaviour, I believe that the MCM can lead to a better lifetime estimation scheme. With some approximation, I discovered that the MCM agrees with the linear extrapolation method for lifetime and activation energy[1,4,51,53,54]. In the case of a one-component model, if the activation energy of a device is known, one could estimate the lifetime of a device at any temperature from the lifetime measurement performed under stress aging[51,53,54]. From Sim's heuristic model[2], the lifetime of a device at any operating temperature with the knowledge of the aging behaviour at an elevated temperature is given by,

$$t_{oper}^{n} = t_{aging}^{n} \frac{\Delta I_{oper}}{\Delta I_{aging}} \exp\left[-\frac{E_a}{nk}\left(\frac{1}{T_{aging}} - \frac{1}{T_{oper}} \right) \right]. \qquad (4.6)$$

For most cases, the estimation requires $\Delta I_{oper} = \Delta I_{aging}$. Using linear extrapolation (n = 1), then

$$t_{oper} = t_{aging} \exp\left[-\frac{E_a}{k}\left(\frac{1}{T_{aging}} - \frac{1}{T_{oper}}\right)\right]. \quad (4.7)$$

Eq. (4.7) was first proposed by Hartman and Dixon[53] and later fully developed by Joyce *et al.*[54] The calculation of E_a is always accomplished by overstressing a device until the transient modes of the device saturate. Then, from measuring threshold degradation at two or more temperatures, the activation energy is given in a linear approach as[53,54]

$$E_a = \frac{kT_1T_2}{T_1 - T_2} \ln\left(\frac{\partial I(T_1)/\partial t}{\partial I(T_2)/\partial t}\right) = \frac{kT_1T_2}{T_1 - T_2} \ln\left(\frac{\Delta I(T_1)}{\Delta I(T_2)}\right). \quad (4.8)$$

It is found that the MCM arrives to the same results in Eqs. (4.7) and (4.8) (see derivation in Sec. 7.2 in Chapter 7), if it is assumed that

$$\exp\left[cn_{th}^2 VM_{nm} t \exp\left(-\frac{E_{am}}{kT}\right)\right] \approx 1 + cn_{th}^2 VM_{nm} t \exp\left(-\frac{E_{am}}{kT}\right). \quad (4.9)$$

Given that the MCM offers correct physics to describe population growth of defects and the approximated MCM provides identical results to the Hartman-Dixon method, it is believed that the MCM is a valid aging model of semiconductor lasers. Hence, the physics in the MCM provides a physical explanation to Eqs. (4.7) and (4.8). However, Eq. (4.9) is an invalid approximation since $cn_{th}^2 VM_{nm} t \exp[-E_{am}/(kT)]$ is significantly larger than 1 in most cases. It is experimentally difficult to verify the Hartman-Dixon method since the verification may require lasers to be aged in the operating condition (e.g. T = 10°C, I_{op} ~ 40 mA, and operating time ~ 25 years +). Furthermore, numerous

testing temperatures for the estimation of E_a will be required with a substantial population size of each setting.

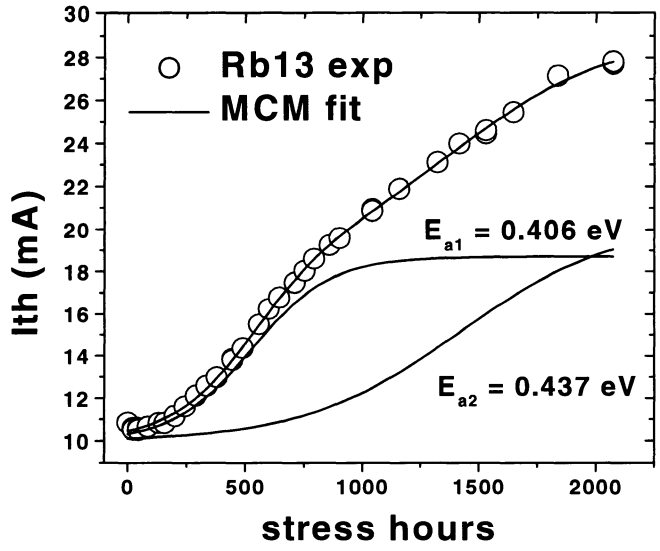

Fig. 4.4. Plots of the aging curve of the Rb13 laser and the MCM fit using $cn_{th}^2V = 50\ cm^3/s$. The corresponding first and second components of the fit are also plotted and labeled with $E_{a1} = 0.406$ eV and $E_{a2} = 0.437$ eV respectively. Please note that the fit components are offset by I_{th0} for clarification.

Conversely, estimations of the device lifetime and activation energy may be obtained through the MCM. Since cn_{th}^2V and E_{am} are degenerate through the combined term, $cn_{th}^2V \exp(-E_{am}/(kT))$, the calculation of E_{am} requires the knowledge of cn_{th}^2V or vice versa. The value of cn_{th}^2V is not known as it has generally not been used in the analyses of aging data. For demonstration purpose, I assumed $cn_{th}^2V = 50$ and fitted Eq. (2.11) to 10 RWG MQW GC DFB lasers to

extract the activation energies. Figure 4.4 shows an example of the MCM fit to one of the 10 lasers and the corresponding MCM components. The fit coefficients of the lasers are recorded in Table 4.2. Only two sets of uncertainties are listed in for laser populations Rb13 and Rd40, for reasons of clarity. Since these ten lasers were already fitted in chapter 2, the same coefficients were used and the activation energies were fit to with them. Therefore, only the activation energies have uncertainties listed.

An interesting case, laser Rd40, was found that its long-term degradation has a smaller activation energy relative to its transient failure modes. Plots of the MCM fit to the Rd40 laser and the corresponding MCM components are shown in Fig. 4.5. Please note that part of the aging curve in Fig. 4.5 between 156 to 447 hours is shifted out of scale due to a systematic error, and the corresponding data points are not shown in the plot. The activation energy of the second component can be seen on Table 4.2 to be less than that of the first component. The shape of the curve has a very distinct knee due to the first component and a very weak long-term degradation that resembles a linear curve from the second component. This kind of shape seems to be a characteristic signature for cases where the second activation energy is smaller than the first activation energy. Furthermore, the shape of the aging curve is similar to the ones reported by Hakki *et al.* [4] So, it may not be an isolated special case. However, a general conclusion cannot be drawn yet since I do not have data that span a longer aging time.

Samples	Rb02	Rb08	Rb10	Rb11	Rb13	Rb15	Rd03	Rd13	Rd20	Rd40	Mean ± S.D.
I_{th0} (mA)	11.40	9.76	9.38	11.46	9.96	11.71	14.82	10.85	11.83	16.79	
$\frac{qV}{\eta_i} A n_{th}$ (mA-cm^3)	0.96	1.30	1.42	0.96	1.07	0.59	0.73	0.62	0.71	0.73	
Scaled M_{n1} (cm^{-3})	9.73	8.79	7.35	4.25	8.14	11.47	1.94	3.19	3.67	9.93	
Scaled $N_{d1}(0)$ (cm^{-3})	0.68	0.86	0.60	0.21	0.33	0.86	0.048	0.27	0.17	0.86	
E_{a1} (eV)	0.412± 0.002	0.417± 0.002	0.406± 0.001	0.381± 0.002	0.406 ± 0.002	0.427± 0.003	0.331± 0.003	0.364± 0.004	0.366± 0.003	0.422 ± 0.003	0.39 ± 0.01
Scaled M_{n2} (cm^{-3})	14.01	8.17	8.13	4.54	9.67	11.46	5.09	3.05	1.85	2.08	
Scaled $N_{d2}(0)$ (cm^{-3})	0.35	0.15	0.21	0.09	0.13	0.31	0.21	0.13	0.05	0.07	
E_{a2} (eV)	0.453± 0.002	0.432± 0.003	0.433± 0.002	0.405± 0.003	0.437 ± 0.003	0.448± 0.005	0.408± 0.003	0.391± 0.007	0.370± 0.009	0.393 ± 0.029	0.42 ± 0.01
$E_{a1} - E_{a2}$ (eV)	0.041	0.015	0.027	0.024	0.031	0.021	0.077	0.027	0.004	0.03	0.024 ± 0.008

Table 4.2. Fitting of E_a's with $cn_{th}^2 V = 50\,cm^3/s$. The calculated mean values and standard deviations of the mean activation energies are listed on the last column.

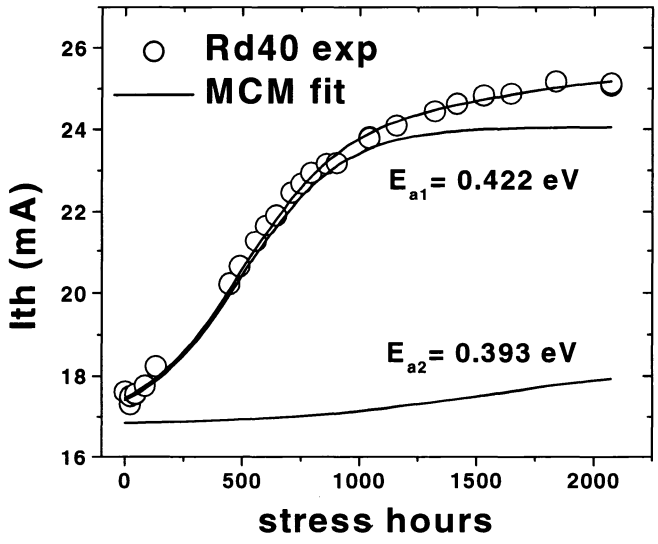

Fig. 4.5. Special case where the second component has lower activation energy than the first component. The corresponding first and second components of the fit are also plotted and labeled with $E_{a1} = 0.422$ eV and $E_{a2} = 0.393$ eV respectively. Please note that the fit components are offset by I_{th0} for clarification.

From the assumption that $cn_{th}^2V = 50$, the mean values of E_{a1} and E_{a2} for Rd40 are calculated to be 0.422 eV and 0.4393 eV with standard deviation of the mean (i.e., the sample standard deviation divided by the square root of the number of samples) of 0.01 eV and 0.01 eV respectively (see Table 4.2). The question is, are the two activation energies different. In Table 4.2, a list of differences of the pair of activation energies in each column has been constructed. It can be

determined, using a paired sample *t*-test, if the calculated activation energies are significantly different. The *t* ratio[55] is defined as

$$t = \frac{(E_{a1} - E_{a2})_{mean}}{S_{mean}} = 2.81 \tag{4.10}$$

where $(E_{a1} - E_{a2})_{mean} = 0.024$ is the mean of the difference and $S_{mean} = 0.008$ is the standard deviation of the mean (or the standard error). The critical value for a two-tailed test at a confidence level of 95 % with 9 degrees of freedom is 2.26, which is less than the *t* ratio calculated in Eq. (4.10). In other words, with more than 95 % confidence, the fitted activation energies corresponding to two individual components are not the same.

In principle, one could utilize Hartman and Dixon's idea[53] to obtain E_{am} by fitting the MCM to two groups of identical devices aged with the same biased current at two different temperatures: T_1 and T_2. Since these are devices from the same parent wafer, the fits from the two groups should produce statistically identical $cn_{th}^2 V$ and E_{am}. Suppose that the fit coefficients $cn_{th}^2 V \exp(-E_{am}/(kT_1)) = \psi_{1,m}$ and $cn_{th}^2 V \exp(-E_{am}/(kT_2)) = \psi_{2,m}$ are obtained, where $\psi_{i,m}$ is a constant obtained from fitting and the subscripts i and m represent the temperature T_i and the m-th component respectively. Then, the activation energy of the m-th component is given as,

$$E_{am} = k\left(\frac{1}{T_1} - \frac{1}{T_2}\right)^{-1} \ln\left(\frac{\psi_{2,m}}{\psi_{1,m}}\right). \tag{4.11}$$

Horikoshi *et al.* [30] and Hakki *et al.* [4] require the estimation of the lifetime using the Hartman-Dixon method to be performed after the saturation of the transient modes, but the MCM has a slightly different treatment of the estimation of lifetime. The MCM requires the knowledge of all the transient modes that cause the laser to fail, and in Sec. 7.2, an analytical expression for the lifetime estimation is presented. For a conservative estimation of lifetime t_2 at the ambient temperature of T_2 with the knowledge of the lifetime t_2 at a different temperature T_1, the MCM's formulation is as follows:

$$t_2 = t_1 \frac{\Delta I_m(t_2, T_2)}{\Delta I_m(t_1, T_1)} \frac{\sum_{m=1}^{\varsigma} N_{dm}(0) M_{nm} \exp\left(-\frac{E_{am}}{kT_1}\right)}{\sum_{m=1}^{\varsigma} N_{dm}(0) M_{nm} \exp\left(-\frac{E_{am}}{kT_2}\right)}. \tag{4.12}$$

Using Rb13 in Table 4.2 as an example, if t_1 = 1000 hours for $\Delta I_m(1000\text{hrs}, 423\ \text{K})$ = 10 mA at 150 °C, then the lifetime t_2 for $\Delta I_m(1000\text{hrs}, 283\ \text{K})$ = 10 mA is calculated to be 262000 ± 7000 hours or 29.9 ± 0.8 years at 10 °C. Since Eq. (4.12) also requires the assumption made in Eq. (4.9), which is not valid in most cases, I expect that the estimated value of t_2 is poor relative to the true value. For comparison purpose, I obtain t_2 = 340857 ± 57 hours numerically from Eq. (2.11) using Maple symbolic calculation software. In this particular case, the estimated lifetime using Eq. (4.12) is about 23 % less than the numerically calculated value of the lifetime, due to the invalid approximation used in deriving Eq. (4.12). Nonetheless, Eq. (4.12) provides an alternative

analytical method for a conservative estimation of lifetime, in addition to the Hartman-Dixon estimation method.

4.4 CONCLUSION

Some of the limitations of the application of a universal aging curve to the analysis of accelerated lifetest analysis of a semiconductor laser have been shown. The basic problems in such an analysis are influenced by level of stress (temperature and current), the neglect of multiple defect-components, and the length of aging time used by the experimenters. These factors play an important role in perturbing the partition between the transient degradation modes which are apparent over a given time window, and in turn, affects the perception of an aging curve in the experimenter's eyes when designing an appropriate aging model for the system. The MCM aging model provides a non-subjective method by which non-linearities in lifetest data can be quantitatively assessed.

Furthermore, the MCM can be used to generate aging curves with shapes similar to results presented in some classic publications on aging.[2,4,30] This demonstration clearly shows that the MCM helps understand the discrepancies that exist between these publications. It was shown that the estimation methods for activation energy and device life suggested by Hartman and Dixon and others can be treated as an approximation to the MCM. Using the MCM, a new method was devised to estimate the activation energy and device life. This new method

can be easily incorporated to standard accelerated lifetesting procedures that involve overstress in temperature and bias current.

CHAPTER 5. CHARACTERIZATION OF DIELECTRIC COATED FACETS OF SEMICONDUCTOR LASERS

5.1 INTRODUCTION

In this chapter, preliminary results of an aging-related degradation of the PL yield from the facets of $SiO_x/Si/SiO_x$ thin film coated InGaAsP/n-InP lasers is reported. A scanning PL topographic technique[56] was utilized to probe the quality of the laser facet. This technique provides a spatial resolution of about 1 μm, which produces a clear map of the spatial variation of the PL yield on the facet of a laser diode. The PL yield was observed to increase continuously under uninterrupted excitation by a HeNe laser source and the observed phenomenon will be termed enhanced PL yield (EPL) from now on. The change of this EPL during aging could be correlated to the degradation of the PL yield, and contributed to an aging-induced spatial inhomogeneity of the PL yield from the facets of the laser diodes. For this reason, the change of EPL was used to measure the quality of the $SiO_x/Si/SiO_x$/InP interface.

RWG MQW GC DFB lasers were used in this study, and the aging process has been discussed in chapter 2. During the course of aging, room-temperature spatially-resolved PL measurements and time-resolved PL measurements were periodically taken in an *ex-situ* station at room temperature (25 °C). All these measurements were taken from the front facets of the lasers, because the structure of the laser module prohibits any close access (< 1cm) to the back of the mounted laser. PL degradation on the facets of over 50 aged lasers

was observed using the spatially-resolved PL technique. For the study of light-induced EPL, a set of time-resolved PL measurements were performed on 8 samples that were aged for 2074 h. All these samples exhibited different degrees of reduction of the PL yield (i.e., PL degradation) under the laser ridge. The threshold current degradation could not be correlated with the facet PL degradation.

The front facets of the examined lasers are covered with an antireflection coating of a 3-layer sandwich type: $SiO_x/Si/SiO_x$ (830/220/830 Å). The coating is deposited on the laser facet by electron cyclotron resonance plasma-enhanced chemical vapour deposition (ECR-PECVD) at 150 °C. The n-side of the laser is bonded down on an AlN heatsink, which is mounted on a ceramic base. The p-up orientation offers the least damage caused by the bonding action on the facet coating at the active region. Therefore, a controlled environment is naturally provided by the p-up orientation to study thermal, current, and optical stress on the coated facet.

5.2 SPATIALLY-RESOLVED PL TOPOGRAPHY

The experimental setup of the spatially-resolved PL technique involves a HeNe laser (MWK industries), optical isolator (OFR I0-2-633-LP), chopper (New Focus 3501), neutral density filter wheel (New Focus 5215), mirror, cold mirror (Melles Griot 03MCS005), objective (Newport M-10X), tilt/rotation stage,

micropositioner (Melles Griot Nanomover 9128-980001), HeNe filter (Melles Griot 03FCG111), rotating polarizer (900 nm Corning Polarcor optical glass polarizer), and Si detector (EG&G C30807E) as shown in Fig. 5.1.

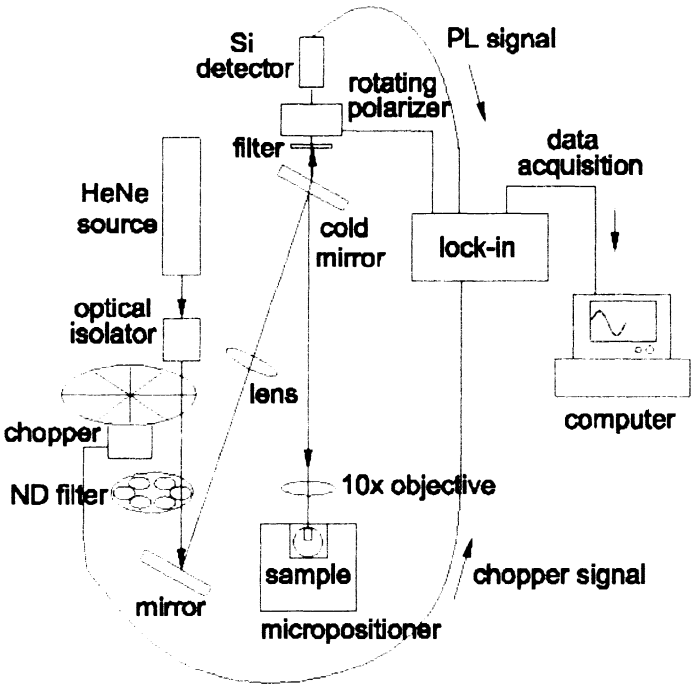

Fig. 5.1. Schematic of the PL system setup.

The measurement proceeds as illustrated in Fig. 5.1. First, light for PL excitation is generated from a HeNe laser source. The light then passes through an optical isolator, is modulated by a chopper, and is attenuated by a neutral density filter. The HeNe light is then redirected through a matching lens for optimizing excitation focus, redirected again by a cold mirror to the laser sample through a 10× objective. Since the laser diode is bonded slightly behind a heatsink, a 10× objective is used to allow more working distance at a cost of

lower resolution. The laser diode sample is mounted on a tilt/rotation stage, which is stationed above a micropositioner. Photoluminescence on the facet of the laser diode is generated by the HeNe excitation and collected by the objective. This PL signal shares the same path as the incoming HeNe light, passes through the cold mirror and a rotating polarizer, and reaches the Si detector at the end. Any excess HeNe light, which is not eliminated by the cold mirror, will be blocked out by a HeNe filter placed in front of the rotating polarizer. The rotating polarizer does not serve an important purpose for this particular study, but it allows the system to measure degree of polarization from the sample PL signal.[57] Finally, the PL signal is triggered by both the chopper signal and rotating polarizer signal, and the filtered signal is then collected by a data-acquisition computer. The purpose of the Melles Griot micropositioner below the sample is for generating a spatially-resolved two-dimensional topograph of the PL yield from the laser facet (optical resolution in the order of 4.5 μm). It also allows accurate access to a point on a laser facet (accuracy of 100 nm).

5.3 EXPERIMENTAL RESULTS AND DISCUSSIONS

5.3.1 Enhanced photoluminescence from SiO_x/Si/SiO_x coated n-InP facet

The experimental results suggest that the SiO_x/Si/SiO_x coating enhances the PL yield from the n-InP substrate. For example, the ratio of the PL intensities of an as-cleaved facet and a SiO_x/Si/SiO_x coated facet is approximately 1:2.5 (see

Fig. 5.2). Please note that the PL intensities were measured at different ND indices and have been normalized according to the scheme in Section 7.3, Appendix C, for comparison. The stronger PL emission from the coated facet is due to an enhanced PL signal that increases with the illumination time. The observed PL, l_{total}, can be generalized into two components:

$$l_{total}(t, t_{ill}) = l_c(t) + l_{EPL}(t, t_{ill}), \tag{5.1}$$

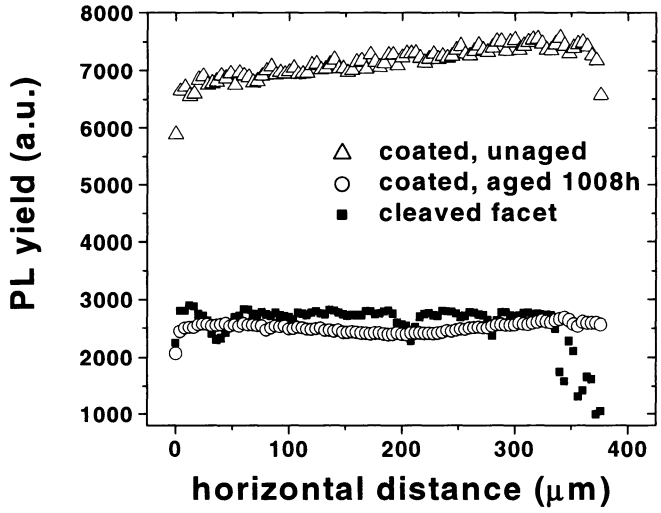

Fig. 5.2. Horizontal PL profiles of a $SiO_x/Si/SiO_x$ coated facet (aged and unaged) and an as-cleaved facet approximately 20 μm below the ridge (laser: Rb DY12).

where $l_c(t)$ denotes the constant detected signal or offset, l_{EPL} denotes the EPL, and t_{ill} denotes the illumination time. To avoid confusion, $l_c(t)$ is assumed constant with illumination time but depends on aging time, t, as shown later. Illumination time always comes with the subscript "ill" while the aging time will

be presented without a subscript. This EPL was observed elsewhere in the past[58,59,60,61,62,63,64] and is normally observed in the PL signal of an InP or GaAs surface in a nitrogen, argon, or hydrogen ambient. However, not all ambients produce enhancement.[62]

It is generally believed that two surface properties are responsible for the enhancement or degradation of the PL yield: the position of the surface Fermi level and the surface recombination velocity.[58,59,60,65,66] The surface Fermi level is generally pinned due to the existence of localized surface states within the bandgap. Since the surface Fermi level is generally not equal to the bulk Fermi level, a space-charge region or band bending exists at the surface[67] (see Fig. 5.3).

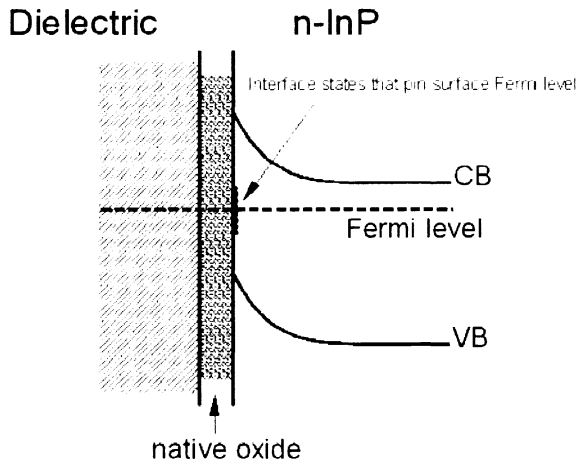

Fig. 5.3. Space charge region at the surface of a dielectric coated n-InP substrate.

The electric field in the space-charge region pushes the minority carriers to the surface to recombine nonradiatively, and hence radiative recombination is reduced. The surface passivation helps unpin the surface Fermi level and moves

the band at the surface towards the flat band condition. As the band bending is minimized, the number of nonradiative recombination events at the surface by minority carriers is reduced accordingly.[59,66] An alternative model[58,59] has also been proposed that the space-charge region separates the photogenerated electron-hole pairs and leads to a reduction in radiative recombination efficiency near the surface. Similarly, the reduction of the space-charge region enhances the near-facet radiative recombination efficiency in this model. There exist other more complex models[68,69] on the PL change due to the surface Fermi level shifting, but will not be discussed in this chapter. The surface recombination velocity (S in cm/s) describes the nonradiative recombination pathway at the surface, and can also be reduced by removing surface states or impurities through surface passivation.

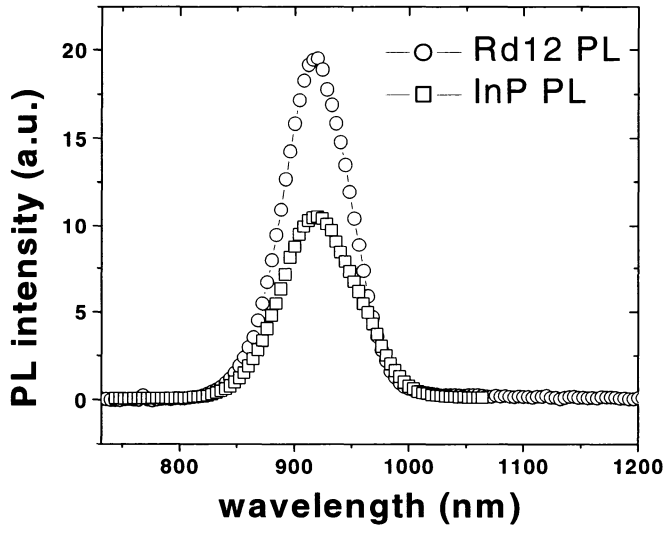

Fig. 5.4. Room temperature spectra of the coated n-InP from the sample Rd12 (circle) and a plain n-InP cleaved facet (square).

To verify that the enhancement is due to an improvement of the surface quality, a spectral measurement was performed on a coated facet and a cleaved facet, respectively. Figure 5.4 shows the spectrum of a coated n-InP facet (Rd12) compared to that of a cleaved n-InP facet. The shapes of the coated facet and the uncoated facet in this case are similar except the coated one produces higher PL yield as expected, and both peak at around 920 nm. The observation supports the claim that the enhanced PL on the coated facet is due to the reduction of the surface recombination rate. Without passivations, it will be seen later that the photoluminescence from the InP surface generally decays due to recombination enhanced defect formation in an air ambient.

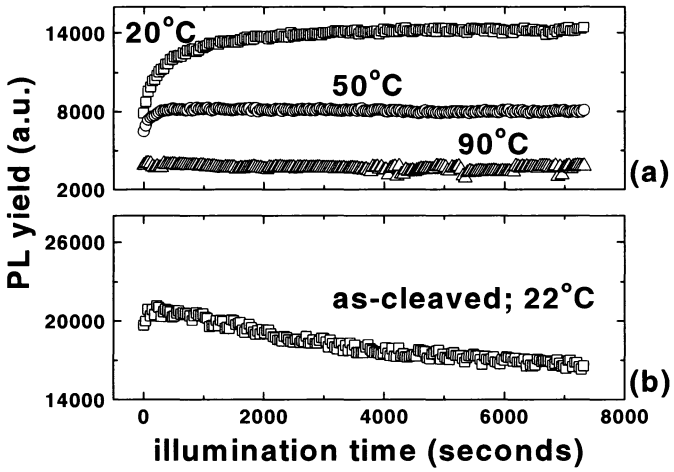

Fig. 5.5. (a) temperature dependence of PL yield as a function of illumination time on a coated facet (Rd L21). (b) PL yield as a function of illumination time on an as-cleaved facet (Rb DY25).

The EPL is observed as an increasing photoluminescence yield when excited continuously by a laser source with photon energy larger than the bandgap of the material. From the measurement of PL yield versus illumination time at different temperatures above 20 °C (see Fig. 5.5(a)), the observed EPL decreases rapidly with temperature, and the detected PL eventually exhibits degradation with illumination time which resembles the case where PL degrades on an as-cleaved n-InP substrate in air[62,63] (see Fig. 5.5(b)). The decrease of the PL observed in Fig. 5.5(a) is thought to be caused by recombination enhanced defect reaction (REDR),[70,71,72] and an increase of Auger recombination rate. Excitation-enhanced oxidation on the crystal surface has been dismissed as the cause of the observed long-lasting PL degradation.[71,73]

The passivation observed through EPL is reversible as in the case of molecular-adsorption passivation reported by others.[59,62,64] The passivation adsorbate and the enhancement mechanism in this case are unknown. Figure 5.6 presents the observed EPL results measured in air at a spot on the laser facet measured over 21 h after excitation by a focused HeNe laser beam on one spot for 2 h. One can see the excess or enhanced PL yield from the spot slowly degraded with time and almost restored to the same normal PL level as the surrounding area after 21 h. The yield of the EPL is proportional to the illumination time and the power density, and saturates eventually. Therefore, the focused HeNe excitation due to the scanning of the image (~ 1 s per location) and the perturbation due to room light are negligible compared to a focused HeNe excitation that lasts for 2 h.

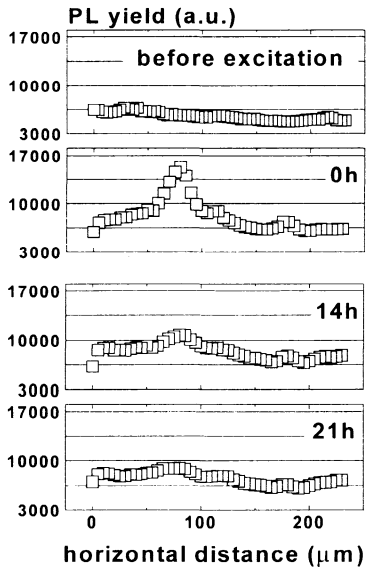

Fig. 5.6. Time evolution of the enhanced photoluminescence shown as horizontal profiles before excitation and at 0 h, 14 h, and 21 h after a 2-h HeNe laser excitation at about 40 μm from the top (laser: Rd L02).

5.3.2 PL degradation on aged $SiO_x/Si/SiO_x$ coated n-InP facets

Figure 5.7 presents the facet PL topographs of a laser at the stage (a) unaged, (b) aged, (c) facet coating etched off by diluted HF (12.5%), and (d) the enhanced image of (b). The intensity chart is located beside the false-colored image, where red, green, and blue represent low, medium and high intensity respectively. Please note that the aspect ratio of the facet images is modified to enhance the viewing of the PL degradation. The PL yield is rather uniform in

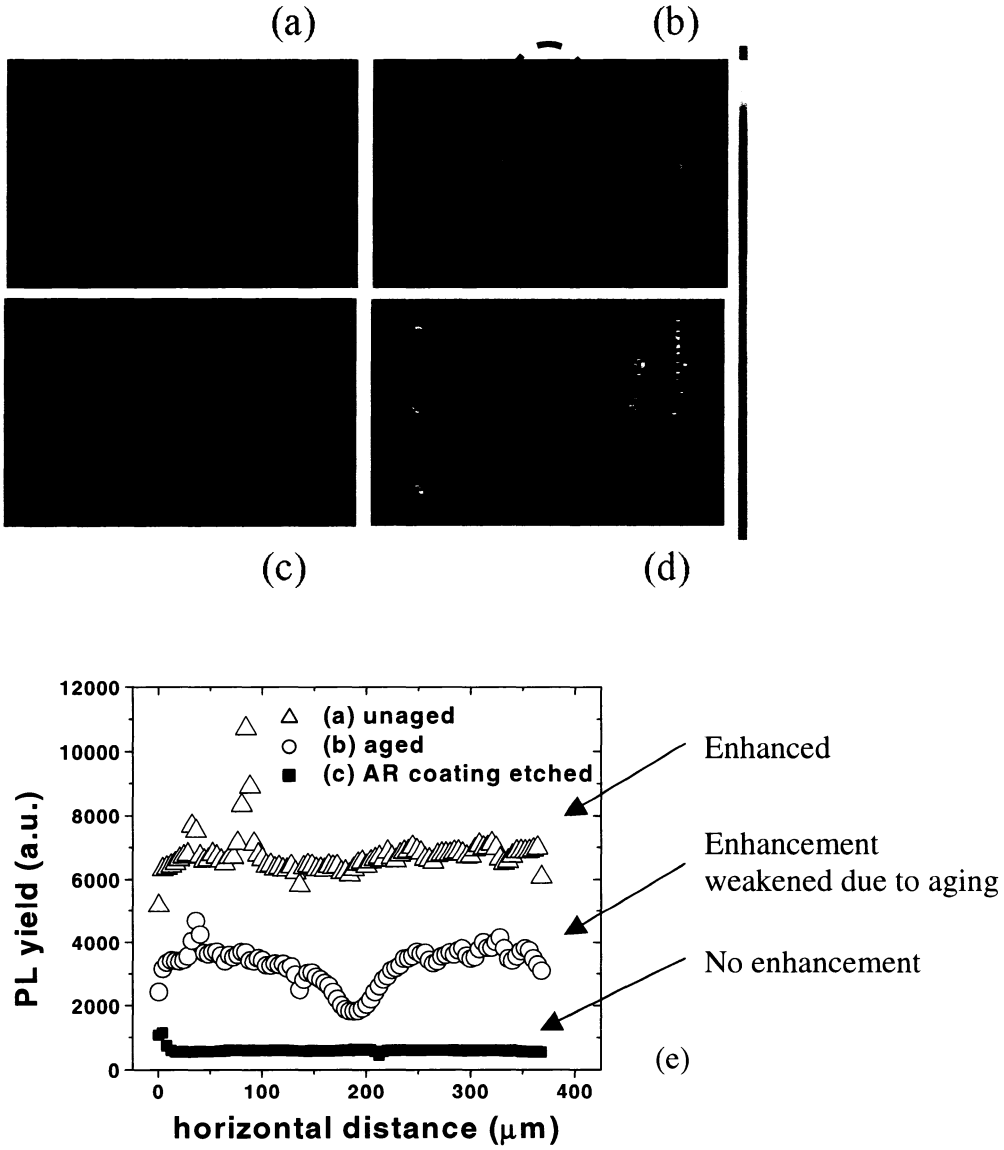

Fig. 5.7. False-colored image of a single device (Rd DY11) active up (a) unaged; (b) aged; (c) etched; (d) same as (b) except the values of the picture is scaled and offset as a higher value to enhance the hydrogen effusion path pattern created by the joule heating of the bias current; (e) horizontal PL profiles near the ridge comparing the cases in (a), (b), and (c). Note: the arc at the bottom is a solder blob.

the unaged stage as shown in Fig. 5.7(a), except for the blue dots (higher PL yield) that trace out a pair of crossed vertical lines. These blue dots occurred as a result of an alignment process, where PL signals from the top and bottom of the laser and from the left and right ends of the laser were measured to ensure that the facet was perpendicular to the HeNe beam. In Fig. 5.7(b), one can see PL degradation at the active region (center and top region), which is highlighted by a circle. The severe PL degradation under the ridge is believed to be caused by higher temperature experienced at the active region during aging. In fact, one can offset the value on the map to enhance the viewing of a PL-degraded region in Fig. 5.7(d). To show that this PL degradation was only an effect exhibited by the facet coating, the laser was etched by diluted HF (12.5%) for 8 minutes in a ultrasonic bath. The ultrasonic bath helped remove the amorphous Si layer mechanically since it resists HF. The resulting PL topograph is shown in Fig. 5.7(c), where the PL yield becomes uniform again. Three horizontal profiles for the unaged, aged, and etched facets, respectively, are shown in Fig. 5.7(e). If one compares the etched PL level to the as-cleaved PL level (see Fig. 5.7(e) and Fig. 5.2), it appears that the HF etching removes the PL enhancement and reduces the PL yield of an etched facet to the level expected from an as-cleaved facet. This suggests that the PL degradation at the ridge shown in Fig. 5.7(b) and (e) indicates a weakened passivation effect at the ridge as opposed to an enhanced growth of surface defects at the ridge. Furthermore, it is evident from Fig. 5.7(e) that the passivation of the InP surface came from the coating since the removal of the

coating eliminated the enhancement. One possible candidate that can be employed as a passivation agent is hydrogen[58,74,75] that exists in the $SiO_x/Si/SiO_x$ coating. However, it is extremely difficult to identify the true passivation agent.

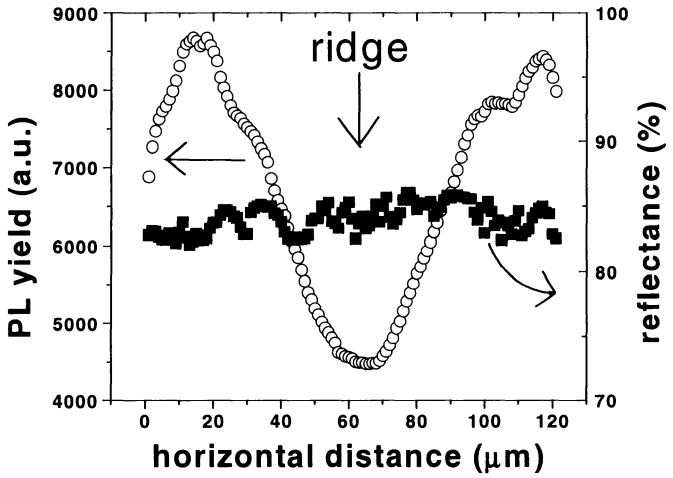

Fig. 5.8. The PL and reflectance profiles of a laser about 15 μm under the ridge. The label "ridge" indicates where the ridge is located with respect to the profile.

Besides the increased surface recombination velocity, it is also a concern if this PL degradation signifies a change of the facet reflectivity. The relationship between this PL degradation on the coated facet and the corresponding facet reflectance was investigated, and the result is presented in Fig. 5.8. The facet reflectance was measured using the same scanning PL setup in Fig. 5.1 with the HeNe filter replaced by a hot mirror (Melles Griot 03MHG007) that rejects the PL signal but allows the reflected HeNe light (632.8 nm) to pass. With a micropositioner under the sample, the corresponding facet reflectance after a PL topographical measurement can be accurately mapped out. The PL degradation at

the ridge is recognized as a "dip" in the PL profile in Fig. 5.8, while the corresponding reflectance profile is uniform across the facet. In this case, the PL degradation did not correlate with the reflectance.

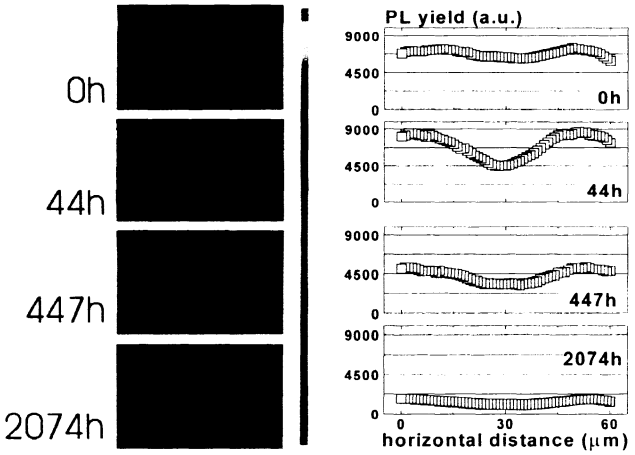

Fig. 5.9. Time evolution of PL degradation under the ridge (left: false-colored PL topographs; right: PL horizontal profiles) of sample Rb05. Dimension: 60 μm (width) by 30 μm (height).

The change of the PL as a function of aging time was investigated to provide a measure of the stability of the coated facet. Figure 5.9 presents a time evolution of the PL topograph right under the ridge in area of 60 μm (width) by 30 μm (height). Again, blue, green, and red denote high, medium, and low yield of PL respectively. Examining the PL profile at 0 h in Fig. 5.9, the PL degraded slightly at the center (slightly rounded bottom) probably due to some occasional operations prior to aging. In the first 44 h, the PL is at the ridge quickly degraded

and formed a "dip" in the PL profile. The "dip" continued to broaden after 447 h of aging, which signifies a spreading of PL degradation. At 2074 h, the "dip" disappeared because the width of the dip actually extended beyond the width of the window (60 μm).

5.3.3 Lifetime estimation

The EPL effect was observed to degrade quickly during the course of aging in comparison with the degradation of the offset PL yield (see Fig. 5.10(a) and (b)). In other words, the passivation on a single spot (regardless of the location) was stronger before aging than after aging. Comparing Fig. 5.10(a) and (b), the enhancement was stronger near the center of the facet than at the ridge. This observation, again, supports the claim that the observed PL degradation at the ridge was caused by the weakened passivation. The decaying curve or rising curve of the detected PL as a function of time could be fitted by a stretched exponential function:[76,77,78,79]

$$I_{EPL}(t, t_{ill}) = \Delta I_{EPL} \exp[-(t_{ill} / \tau_{EPL})^{\beta}] \tag{5.2}$$

and

$$I_{EPL}(t, t_{ill}) = \Delta I_{EPL} \{1 - \exp[-(t_{ill} / \tau_{EPL})^{\beta}]\} \tag{5.3}$$

respectively, where ΔI_{EPL} gives the magnitude of decay and enhancement,

$$\tau_{EPL}(T) = \tau_{EPL}(0) \exp[E_{EPL} / (kT)], \tag{5.4}$$

and β is a characteristic constant which is larger than zero.

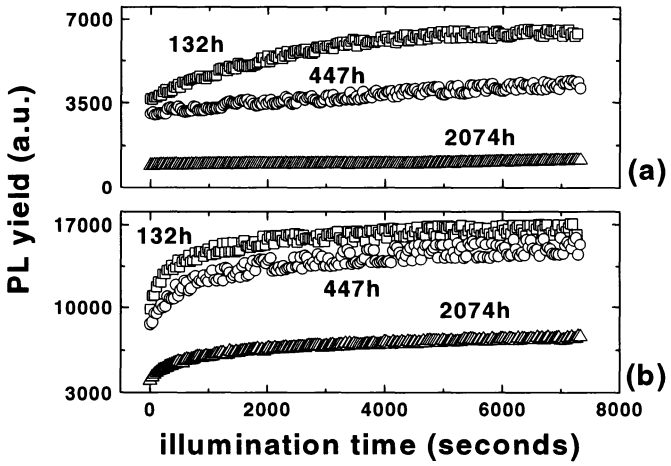

Fig. 5.10. Time evolution of the PL growth curve as a function of illumination time at132 h, 447 h, and 2074 h of aging of sample Rb05: (a) near ridge, and (b) near center of the chip, well away from the ridge.

However, as the PL-illumination time curve degraded during aging, the PL-illumination time curve did not rise as a simple stretched exponential function but sometimes started to decay after a period of illumination time (see Fig. 5.5). In order to quantify the amount of EPL through a consistent scheme, the area under the observed EPL over 7200 s was integrated, instead of fitting the curve with the stretched exponential function. As a matter of fact, Bube[80] interpreted the area under the growing PL curve as an indicator of the density of trapped carriers in the material. A physical quantity called integrated EPL, L_{EPL}, is defined for the purpose of quantifying the EPL effect:

$$L_{EPL}(t, t_{ill}^{i}, t_{ill}^{f}) = \int_{t_{ill}^{i}}^{t_{ill}^{f}} l_{EPL}(t,p)\,dp \tag{5.5}$$

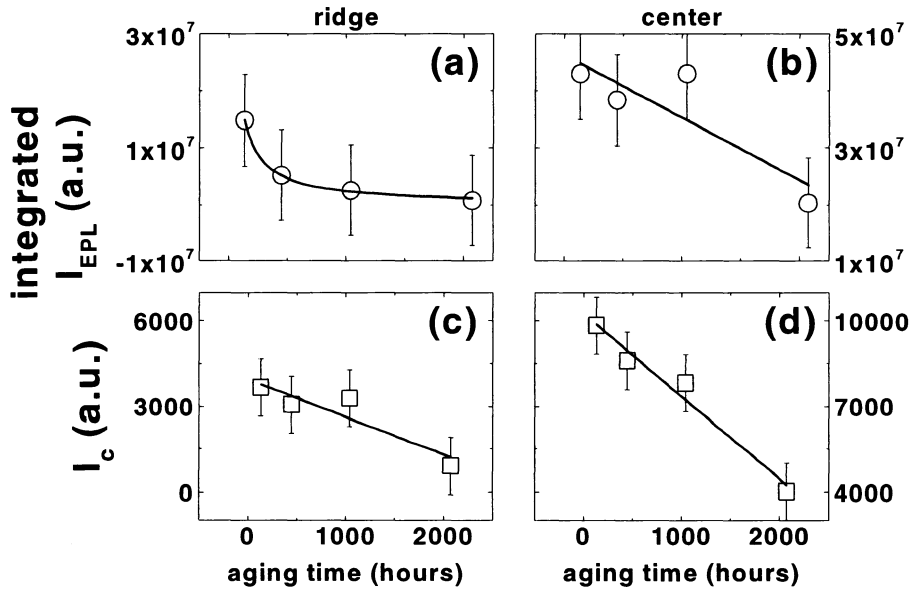

Fig. 5.11. L_{EPL} (top row: (a) and (b)) and l_c (bottom row: (c) and (d)) as a function of time at the ridge (left column: (a) and (c)) and near the center of the facet (right column: (b) and (d)) of sample Rb05.

where $l(t_{ill})$ denotes the measured PL yield at illumination time t_{ill}, and t_{ill}^{i} and t_{ill}^{f} denote the initial and final times respectively. Please note that $l(t_{ill}^{i}) = l_c$ where l_c is a function of aging time, and it is subtracted from the integrated EPL. Therefore, the integrated EPL only measures the effect of the passivation on the PL assuming Eq. (5.1) is valid.

Since the EPL measures the degree of passivation or the quality of the facet, it can be utilized as a probe of the facet stability during aging. Figure 5.11 shows the time evolution of the integrated EPL and the l_c from 132 h to 2074 h. The top row corresponds to the integrated EPL near the ridge (Fig. 5.11(a)) and near the center of the facet (Fig. 5.11(b)). The scales of EPL are unified for both the ridge and center plots using the method in Appendix C. The bottom row, Fig. 5.11(c) and (d), correspond to l_c at the ridge and the center respectively. As expected that the rate of degradation is thermally activated, the higher joule heating, current density, and light intensity at the ridge cause the EPL at the ridge to degrade faster during aging (see Fig. 5.11(a)) as compared to the EPL near the center of the facet (Fig. 5.11(b)). Moreover, I found that the decaying EPL near the ridge fits best (in terms of the measured variance of the fit) with a bimolecular decaying function[80]:

$$L_{EPL}(t) = L_{EPL}(0)/(1 + t / t_{halflife}), \tag{5.6}$$

where t denotes the aging time and

$$t_{halflife} = t_c \exp[E_c/(kT)] \tag{5.7}$$

denotes the aging time where the L_{EPL} is reduced by half. Equation (5.6) is derived from the bimolecular rate equation:

$$dL_{EPL}(t)/dt = -L_{EPL}^2(t)/(L_{EPL}(0)\, t_{halflife}). \tag{5.8}$$

	Ridge: bimolecular degradation $L_{EPL} = L_{EPL}(0)/(1+t/t_{halflife})$			Center: linear degradation $L_{EPL} = L_{EPL}(0)(1-t/t_{fulllife})$		
Samples	$L_{EPL}(0)$ (a.u.)	$t_{halflife}$ (hours)	χ_ν^2	$L_{EPL}(0)$ (a.u.)	$t_{fulllife}$ (hours)	χ_ν^2
Rb02	...	...	...	$4.91\text{x}10^7$	5035	0.70
Rb04	...	...	...	$5.05\text{x}10^7$	3725	0.67
Rb05	$6.92\text{x}10^7 \pm 1.91\text{x}10^7$	36 ± 14	0.002	$4.62\text{x}10^7 \pm 0.53\text{x}10^7$	4236 $\pm$ 2094	0.69
Rb06	$2.59\text{x}10^7$	299	0.03	$4.82\text{x}10^7$	6036	1.60
Rb07	...	...	...	$2.24\text{x}10^7$	3510	0.05
Rd03	...	...	...	$5.09\text{x}10^7$	4012	0.47
Rd13	$2.50\text{x}10^7$	654	0.05	$4.76\text{x}10^7$	8479	2.62
Rd39	$2.36\text{x}10^7$	1900	1.23	$4.29\text{x}10^7$	9587	2.21
	Average $3.59\text{x}10^7 \pm 2.22\text{x}10^7$	MTTF N.A.		Average $4.47\text{x}10^7 \pm 0.94\text{x}10^7$	MTTF 6176 $\pm$ 48	

Table 5.1. Fitted parameters of the bimolecular degradation (ridge) and linear degradation (center) for the measured integrated EPL.

The parameters, t_c and E_c, in Eq. (5.7) represent the characteristic aging time when temperature T goes to infinity and the activation energy for the degradation of the coating respectively. For the sample Rb05 in Fig. 5.11(a), the $t_{halflife}$ is estimated to be 36 ± 14 h (see sample Rb05 in Table 5.1), based on the fitting of Eq. (5.6). Please note that the χ_ν^2 in this case is given by the calculated variance divided by the square of an estimated error. By inspection, I estimated the error for the measured PL is 1000 for the offset and 500 for above the offset. Using error propagation formula, I found that the calculated error for the integrated EPL is 8×10^6. Since the fit is good, our estimated error for the integrated EPL may be too large and causes the χ_ν^2 to be 0.002 which is << 1. I attribute this small χ_ν^2 to

the overestimation of error (i.e., $\Delta l = 1000$) rather than an improper fitting of model.

In Table 5.1, only 4 out of 8 samples (Rb05, Rb06, Rd13, and Rd39) were observed to exhibit decaying behaviour for the EPL at the ridge beyond 132h. The other 4 samples (Rb02, Rb04, Rb07, and Rd03) seemed to exhibit an already degraded EPL at the ridge at 132h where the integrated EPL had reached the bottom value and appeared constant over aging time. No values are recorded for these fully degraded films since the EPL measurements prior to 132 h are not available. The initial values $L_{EPL}(0)$ are assumed to be normally distributed, whereas $t_{halflife}$ and $t_{fulllife}$ are assumed to follow lognormal distribution. The mean time to failure (MMTF) can be estimated from $t_{halflife}$ and $t_{fulllife}$ using the following set of formulas[81]:

$$MTTF = T_{50} \exp(\sigma^2 / 2) \tag{5.9}$$

$$SD_{MTTF} = T_{50} \exp(\sigma^2) * [\exp(\sigma^2) - 1] \quad . \tag{5.10}$$

where

$$\sigma = \ln\left(\frac{T_{50}}{T_{15.9}}\right). \tag{5.11}$$

By fitting a straight line to log-log plot of the fulllife measurements versus the cumulative failure, T_{50} and $T_{15.9}$ can be estimated by the fitted straight-line equation at 50 and 15.9 % cumulative failure respectively. The MTTF corresponding to $t_{halflife}$ is not calculated in Table 5.1, because too few data points

are involved and the corresponding error are too large to present a reasonable result.

What caused the ridge coating to exhibit an anomalous rapid degradation is not known, but this rapid facet PL degradation did not necessarily cause the lasers to degrade faster. In other words, the PL degradation did not have a significant impact on the reliability of the device. The EPL near the center of the facet decayed so slow that it appeared to be linear, but a bimolecular decay would be expected if the aging was to be performed for a longer time. This linear decay was modeled using the Taylor-series approximated version of Eq. (5.6):

$$L_{EPL}(t) = L_{EPL}(0)/(1 + t/t_{halflife}) \approx L_{EPL}(0)(1 - t/t_{fulllife}). \quad (5.12)$$

Since the term $t_{halflife}$ now depicts the fact that L_{EPL} becomes zero as as t_{aging} equal to $t_{halflife}$, I define it as $t_{fulllife}$ instead. Please note that if the decay was supposed to be bimolecular, then $t_{fulllife}$ estimated by Eq. (5.12) must be less than the true $t_{halflife}$ estimated by Eq. (5.6).

The average integrated EPL at t = 0 are $(3.59 \pm 2.22) \times 10^7$ and $(4.47 \pm 0.94) \times 10^7$ for measurement from the ridge and from the center respectively (see Table 5.1). A *t* ratio[32], as in Eq. (2.22), was constructed,

$$t = \frac{\bar{L}_{EPL}^{center}(0) - \bar{L}_{EPL}^{ridge}(0)}{S_p\sqrt{1/N_{center} + 1/N_{ridge}}}, \quad (5.13)$$

where

$$S_p^2 = \frac{(N_{center} - 1)S_{center}^2 + (N_{ridge} - 1)S_{ridge}^2}{N_{center} + N_{ridge} - 2}. \quad (5.14)$$

For the sample sizes, $N_{center} = 8$ and $N_{ridge} = 4$, standard deviations, $S_{center} = 0.94 \times 10^7$ and $S_{ridge} = 2.22 \times 10^7$, the calculated *t* ratio is 0.99. The critical value for a two-tailed test at a confidence level of 95% with 10 degree of freedom is 2.23, which is much larger than the calculated *t* ratio. The average integrated EPL at t = 0 are statistically indifferent between the ridge and the center of the facet. In conclusion, the light-induced PL enhancements between the ridge and the center of the facet are equal. If this enhancement is caused by passivation, then the passivation effect is the same at the ridge or at the center of the facet regardless of the PL offset.

The l_c measurements in Fig. 5.11(c) and (d) show an apparent linear degradation for both ridge and center l_c (the true decay function is not known due to the short aging time). For comparison purpose, the l_c aging curve was fitted with a linear decay function similar to Eq. (5.12):

$$l_c(t) = l_c(0)(1 - t / t_{fulllife}), \quad (5.15)$$

where the term l_c denotes the PL offset. The results of the fitted parameters are recorded in Table 5.2.

	Ridge $l_c = l_c(0)(1 - t/t_{fulllife})$				Center $l_c = l_c(0)(1 - t/t_{fulllife})$			
Samples	$l_c(0)$ (a.u.)	$t_{fulllife}$ (hours)	Rank	χ_ν^2	$l_c(0)$ (a.u.)	$t_{fulllife}$ (hours)	Rank	χ_ν^2
Rb02	3757	4748	12	0.57	11794	4011	5	1.20
Rb04	3818	3265	2	0.13	9479	4306	8	1.82
Rb05	3962 ± 478	2969 ± 988	1	0.36	10249 ± 407	3537 ± 484	3	0.26
Rb06	4125	3802	4	0.14	12950	4017	6	0.50
Rb07	3502	4979	13	0.10	5794	4481	10	0.72
Rd03	...	...	...	...	12781	5208	15	8.26
Rd13	4697	4518	11	0.21	14401	5107	14	2.69
Rd39	5328	4227	7	1.35	12368	4426	9	2.24
	Average 4170 ± 633	MTTF 4263 ± 22	W_1 50		Average 11227 ± 2689	MTTF 4488 ± 13	W_2 70	

Table 5.2. Fitted parameters of the linear degradation (left: ridge; right: center) for the measured $l_c(t)$.

Using Eqs. (5.13) and (5.14), the *t*-ratio for comparing the average $l_c(0)$ from the ridge and from the center of the facet in Table 5.2 is 6.75 (which is larger than the critical value 3.012 at 99% confidence level for a two-tailed test with 13 degrees of freedom), and this implies that $l_c(0)$ from the center is higher than $l_c(0)$ from the ridge. This observation matches our expectation because the ridge area is near the top surface, where surface effects and strain induced by metallization can degrade the PL yield. Furthermore, the ridge may suffer additional PL degradation owing to the existence of the active layer which is a great source of defects, and these defects can propagate and multiply by joule heating, strain, high current density, and intense light power. Therefore, the $l_c(0)$

level from the substrate near the ridge should show less luminescent efficiency relative to the center.

The degradation of the $I_c(t)$ from the InP substrate can be explained by the formation of aging-induced defects which are triggered by electric current, electric field, elevated temperature, and electron-hole recombination. Assuming $t_{fulllife}$ follows lognormal distribution and defines the failure time, the MTTF for the ridge and the center can be calculated using Eqs. (5.9), (5.10), and (5.11) to be 4086 ± 13 and 4391 ± 9 h, respectively. The $t_{fulllife}$ for the ridge and center can be compared in this case. Since $t_{fulllife}$ do not follow a normal distribution, Mann-Whitney test[82] (or Wilcoxon test) is employed. Rank sums of the $t_{fulllife}$ for the ridge and the center are tabulated in Table 5.2 and denoted as W_1 and W_2, respectively. A set of U statistics can be constructed as follows:

$$U_i = W_i - \frac{n_i(n_i+1)}{2} \tag{5.16}$$

where i = 1 or 2. U_1 is conventionally chosen as the smaller U statistic of the two populations, and is equal to 22 in this case. A $w_{1-\alpha/2}$ parameter for hypothesis testing at a level of significance $\alpha = 0.05$ in a two-sided test can be constructed as,

$$w_{1-\alpha/2} = n_1 n_2 - w_{\alpha/2} \tag{5.17}$$

where $n_1 = 7$ and $n_2 = 8$ are sample size of the two populations respectively. For $\alpha = 0.05$, $w_{0.025}$ is equal to 11 and $w_{0.975}$ is equal to 45.[83] Since U_1 is bounded

between $w_{0.025}$ and $w_{0.975}$, $t_{fulllife}$ for the ridge and center are statistically indifferent to a confidence level of 0.95.

5.4 CONCLUSION

Preliminary results of PL measurements using spatially-resolved and time-resolved scanning photoluminescence techniques are presented to examine the EPL effect in the coated facet. The techniques allow one to map the degree of degradation of PL on a coated facet and to probe the stability of a particular location on the facet during the course of aging. The observed localized PL degradation on the laser facet was explained by a decrease of passivation with aging time. The passivation resulted in reduced band bending and/or reduction in surface recombination velocity.

The EPL depended on the ambient temperature and degraded as the laser aged. The change of the EPL is a reliability issue because it reflects the change of the surface recombination rate and thus affects the threshold current. However, the change of the EPL does not affect the facet reflectance significantly. More studies are needed to elucidate the physical mechanism behind the degradation of EPL.

CHAPTER 6. CONCLUSION AND FUTURE WORK

In this thesis, a multi-component model is presented for describing the change of threshold current as a function of aging time. The MCM is separated into two cases: with annealing and without annealing. Comparisons of the MCM with other existing degradation models are presented to provide readers the advantages to adopt this new model. An MCM-comparable lifetime estimation scheme is introduced in Chapter 4, and a comparison with the Hartman-Dixon lifetime estimation scheme is also presented. The possibility to use PL topography to probe the surface stability is explored. A thorough aging study of the coated n-InP surface on a lifetested laser is presented to support the facet PL study.

For future work, there have been a few on-going projects related to the present topic that has not been included in this thesis. The first one is the study of the aging effect on differential quantum efficiency (DQE). Aging study on DQE is rarely discussed in literatures, but it is as important as the threshold current when it comes to evaluating the performance of a laser. In this on-going project, the possibility to incorporate the MCM model in the degradation of DQE is explored.

During the long-term aging study of the laser facet presented in Chapter 5, the degree of polarization (DOP) was also measured from the facet in addition to the PL signal. The in-course monitoring of the DOP during aging allowed observations of the bonding strain relaxation[84] and the p-metallization strain

relaxation. On a p-up laser diode, the strain on the p-side induced by Ti/Pt/Au metallization was found to relax quickly within the first 132h of aging. On the other hand, the significant relaxation on the bonded n-side (Ni/Ge/Au on AuSn solder) could only be observed after 132h of aging. The reason on why there is a time-lag on the strain relaxation of the bonding is still an open question.

Since the MCM can quantify the components of degradation mechanisms, it is possible to identify these components in the laser diode through a carefully controlled large-scaled experiment. The idea can be implemented by collaborating with the McMaster molecular beam epitaxy group. A set of multi-quantum well lasers could be grown using MBE. Defects can be carefully implanted on one set of these MBE-grown lasers. The aging behaviour of this set of lasers can be compared with a control group to reveal the underlying degradation mechanisms of the implanted defects. The use of transmission electron microscopy (TEM) and auger electron spectroscopy (AES) allow one to study how the structure and chemical compositions change in these implanted defects in relation to the formation of defect complexes and networks.

CHAPTER 7. APPENDICES

7.1 APPENDIX A

In this section, the derivation of Eq. (2.7) is presented. One should start from Eq. (2.6),

$$\frac{dN_d(t)}{dt} = [K_n + C_n]N_d(t)\left[1 - \frac{C_n V}{K_n + C_n} N_d(t)\right]. \tag{A.1}$$

Let M_n equal to $(K_n + C_n)/(C_n V)$, then Eq. (A.1) becomes

$$\frac{dN_d(t)}{dt} = C_n V M_n N_d(t)\left[1 - \frac{N_d(t)}{M_n}\right]. \tag{A.2}$$

K_n and C_n depend only on the aging carrier density, n, the activation energy, E_a, and the aging temperature, T, which are assumed to be constant under accelerated aging. Therefore, M_n is constant with N_d and t. Rewriting Eq. (A.2) in the following form and integrate,

$$\int_{N_d(0)}^{N_d(t)} \frac{dN_d(\xi)}{N_d(\xi)\left[1 - \frac{N_d(\xi)}{M_n}\right]} = \int_0^t C_n V M_n \, d\xi. \tag{A.3}$$

Using the method of partial fraction, Eq. (A.3) Becomes

$$\int_{N_d(0)}^{N_d(t)} \frac{1}{N_d(\xi)} + \frac{1/M_n}{\left[1 - \frac{N_d(\xi)}{M_n}\right]} dN_d(\xi) = \int_0^t C_n V M_n \, d\xi. \tag{A.4}$$

The integration gives

$$\left[\ln\left|N_d(\xi)\right| - \ln\left|1 - \frac{N_d(\xi)}{M_n}\right|\right]_{N_d(0)}^{N_d(t)} = C_n V M_n t. \tag{A.5}$$

Finally, by solving Eq. (A.5) for $N_d(t)$, Eq. (2.7) is obtained.

7.2 APPENDIX B

In this section, the MCM is used to derive the expression for the time to reach failure at room temperature based on the aging data at a stress temperature. From Eq. (2.11), the change of threshold current of the m-th component can be written as,

$$\Delta I_m(t,T) = \frac{qVAn_{th}}{\eta_i} \times \left[\sum_{m=1}^{\varsigma} \frac{M_{nm}N_{dm}(0)}{N_{dm}(0) + [M_{nm} - N_{dm}(0)]\exp\left[-c\, n_{th}^2 V M_{nm} t \exp\left(-\frac{E_{am}}{kT}\right)\right]} - N_{dm}(0)\right]. \tag{B.1}$$

The subscript "m" represents the m-th component. Eq. (B.1) can be simplified by setting $N_{dm}(0)/M_{nm} = 0$ since $M_{nm} >> N_{dm}(0)$, and then expanding $\exp[cn_{th}^2 V M_{nm} t \exp[-E_{am}/(kT)]]$ in the Maclaurin series: $1 + cn_{th}^2 V M_{nm} t \exp[-E_{am}/(kT)] + O(\{cn_{th}^2 V M_{nm} t \exp[-E_{am}/(kT)]\}^2)$. Then, the first-order approximation gives

$$\Delta I_m(t,T) \approx \frac{qVAn_{th}}{\eta_i}\left[\sum_{m=1}^{\varsigma} N_{dm}(0)\left(c n_{th}^2 V M_{nm} t \exp\left(-\frac{E_{am}}{kT}\right)\right)\right]. \qquad (B.2)$$

Note that the truncated Maclaurin series approximation for the exponential is not valid as $t \rightarrow \infty$. To extract E_{am} at $t = t_0$, it is common to measure the change of threshold current at two different temperatures[4,51,53,54], T_1 and T_2. Then,

$$\frac{\Delta I_m(t_2,T_2)}{\Delta I_m(t_1,T_1)} = \frac{\sum_{m=1}^{\varsigma} N_{dm}(0) M_{nm} t_2 \exp\left(-\frac{E_{am}}{kT_2}\right)}{\sum_{m=1}^{\varsigma} N_{dm}(0) M_{nm} t_1 \exp\left(-\frac{E_{am}}{kT_1}\right)}. \qquad (B.3)$$

In the case of one component ($\varsigma = 1$) and measurements performed at the same aging time, i.e., $t_1 = t_2 = t_0$, the activation energy can be solved,

$$E_{a1} = \frac{kT_1T_2}{(T_1 - T_2)} \ln\left[\frac{\Delta I_m(t_0,T_1)}{\Delta I_m(t_0,T_2)}\right]. \qquad (B.4)$$

The lifetime t_2 at temperature T_2 is estimated using Eq. (B.2) from measured t_1 at T_1:

$$t_2 = t_1 \frac{\Delta I_m(t_2,T_2)}{\Delta I_m(t_1,T_1)} \frac{\sum_{m=1}^{\varsigma} N_{dm}(0) M_{nm} \exp\left(-\frac{E_{am}}{kT_1}\right)}{\sum_{m=1}^{\varsigma} N_{dm}(0) M_{nm} \exp\left(-\frac{E_{am}}{kT_2}\right)}. \qquad (B.5)$$

In the case of one component ($\varsigma = 1$), the lifetime t_2 at the same degradation (i.e., $\Delta I_m(t_2,T_2) = \Delta I_m(t_1,T_1)$) becomes

$$t_2 = t_1 \exp\left[\frac{E_{a1}}{k}\left(\frac{1}{T_2} - \frac{1}{T_1}\right)\right]. \quad \text{(B.6)}$$

Eqs. (B.5) and (B.6) are only valid for short aging time and low temperature that keep $cn_{th}^2 VM_{nm} t \exp[-E_{am}/(kT)] << 1$.

7.3 APPENDIX C

The PL yield varies after the ND filters are switch (see Fig. 5.1). The PL response from a sample, in principle, should be identical to the ND filters. However, each ND filter may vary from the manufacturer's specification within a certain margin. Furthermore, in addition to the attenuation attributed by the ND filters, the excitation source is attenuated by a constant value through the use of hot mirror and lenses. Therefore, the PL response was measured from a bulk n-InP sample to create a chart of PL response with respect of the ND indices.

ND	PL (I_{chart}(ND))
0.7	4.829 ± 0.044
0.8	3.472 ± 0.006
0.9	3.399 ± 0.022
1	2.232 ± 0.028
1.04	2.190 ± 0.158
1.1	2.190 ± 0.142
1.2	1.459 ± 0.069
1.3	1.030 ± 0.023
1.4	1.000 ± 0.100
1.5	0.783 ± 0.096
1.54	0.524 ± 0.101
1.6	0.601 ± 0.100
1.7	0.417 ± 0.078
1.8	0.310 ± 0.067

1.9	0.280 ± 0.014
2.0	0.214 ± 0.031
2.04	0.214 ± 0.024
2.1	0.219 ± 0.020
2.2	0.151 ± 0.014
2.3	0.111 ± 0.018
2.4	0.096 ± 0.004
2.5	0.076 ± 0.011
2.54	0.084 ± 0.009
2.6	0.087 ± 0.007
2.7	0.060 ± 0.006
2.8	0.044 ± 0.007
2.9	0.038 ± 0.002
3.0	0.030 ± 0.004

Table C.1. Chart of PL response with ND index.

Since ND index 1.4 is the most often used, it is normalized to 1 for convenience. Please note that at ND 1.4, the incident power is about 13.48 MW/m^2 at 632.8 nm for a 15 mW HeNe laser. A conversion of power from the measured index I(measured ND) to a reference index I(reference ND) is simply:

$$I(\text{reference ND}) = \frac{I_{\text{chart}}(\text{reference ND})}{I_{\text{chart}}(\text{measured ND})} I(\text{measured ND}), \qquad \text{(C.1)}$$

where I_{chart}(reference ND) and I_{chart}(measured ND) are taken from Table C.1. Compared to the manufacturer's specification that I(reference ND) = $10^{-(\text{reference ND})}$, the experimental measurements match well with the manufacturer's specification in the trend, but can deviate significantly for individual ND index (see Fig. C.1). Since the light power at a particular ND filter can differ significantly from the specification, the PL measurements are normalized according to Eq. (C.1).

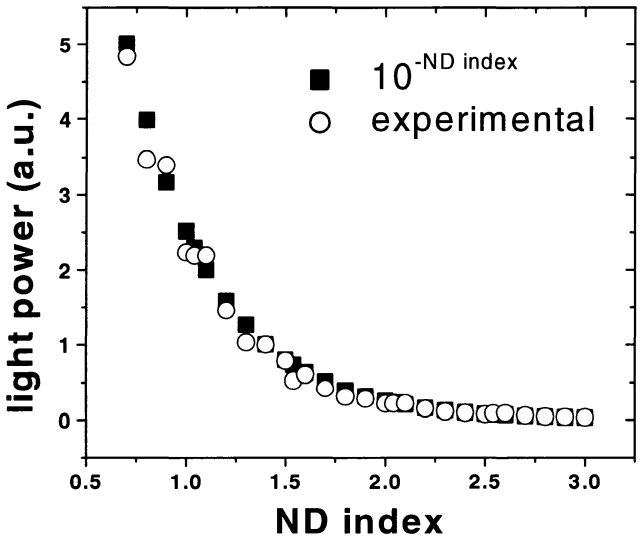

Fig. C.1. Measured light power as a function of ND in comparison to the theory. Estimated uncertainties are smaller than the markers.

CHAPTER 8. REFERENCES

[1] M. Fukuda, *Reliability and Degradation of Semiconductor lasers and LEDs* (Artech House, Boston, 1991), p. 327.

[2] S.P. Sim, *Proc. Semiconductor Device Reliability: Advanced Workshop II, Nato International Scientific Exchange Program, Crete, Greece, June 1989, NATO ASI Series*, vol. 175, A. Christou and B.A. Unger, eds. (Kluwer Academics, Dordrecht, 1990), p. 301.

[3] S.L. Chuang, N. Nakayama, A. Ishibashi, S. Taniguchi, and K. Nakano, IEEE J. Quantum Electron. **34**, 851 (1998).

[4] B.W. Hakki, P.E. Fraley, and T.F. Eltringham, AT&T Tech. J. **64**, 771 (1985).

[5] M. Fukuda, *Reliability and Degradation of Semiconductor lasers and LEDs* (Artech House, Boston, 1991), p. 208.

[6] R.L. Hartman and R.W. Dixon, Appl. Phys. Lett. **26**, 239 (1975).

[7] H. Lu, C. Blaauw, B. Benyon, G.P. Li, and T. Makino, IEEE J. Select. Topics Quantum Electron. **1**, 375 (1995).

[8] O. Ueda, *Defect Control in Semiconductors*, vol. II, K. Sumino, ed. (North-Holland, New York, 1990), p. 1245.

[9] C.H. Henry and D.V. Lang, Phys. Rev. B. **15**, 989 (1977).

[10] P.W. Hutchinson, and P.S. Dobson, Phil. Mag. **32**, 745 (1975).

[11] P.M. Petroff and L.C. Kimerling, Appl. Phys. Lett. **29**, 461 (1976)

[12] S. O'Hara, P.W. Hutchinson, and P.S. Dobson, Appl. Phys. Lett. **30**, 368 (1977).

[13] T. Kallstenius, J. Backstrom, U. Smith, and B. Stoltz, J. Appl. Phys. **86**, 2397 (1999).

[14] S.N.G. Chu, S. Nakahara, L.C. Luther, and H.W. Krautter, J. Appl. Phys. **69**, 6974 (1986).

[15] K. Kondo, O. Ueda, S. Isozumi, S. Yamakoshi, K. Akita, and T. Kotani, IEEE Trans. Electron. Devices, **ED-30**, 321 (1983).

[16] O. Ueda, *Reliability and Degradation of III-V Optical Devices* (Artech House, Boston, 1996), p. 243.

[17] T. Kamejma, K. Ishida, and J. Matsui, Japan. J. Appl. Phys. **16**, 233 (1977).

[18] H. Yonezu, T. Yuasa, T. Shinohara, T. Kamejima, and I. Sakuma, Japan. J. Appl. Phys. **15**, 2393 (1976).

[19] M. Seki, M. Fukuda, and K. Wakita, Appl. Phys. Lett. **40**, 115 (1982).

[20] A.K. Chin, C.L. Zipfel, M. Geva, I. Camlibel, P. Skeath, and B.H. Chin, Appl. Phys. Lett. **45**, 37 (1984).

[21] D. Lisak, D.T. Cassidy, and A.H. Moore, IEEE Trans. Comp. Packag. Technol. **24**, 92 (2001).

[22] R.L. Hartman and A.R. Hartman, Appl. Phys. Lett. **23**, 147 (1973).

[23] D.P. Maki and M. Thompson, *Mathematical Models and Applications* (Prentice-Hall, New Jersey, 1973), p. 313.

[24] C.L. Dym and E.S. Ivey, *Principles of Mathematical Modeling* (Academic, New York, 1980), p. 177.

[25] G.F. Gause, *The Struggle for Existence* (Dover, New York, 1971), p. 50.

[26] P.R. Bevington and D.K. Robinson, *Data Reduction and Error Analysis For The Physical Sciences*, 2nd ed. (McGraw-Hill, New York, 1992), p. 106.

[27] B.R. Frieden, *Probability, Statistical Optics, and Data testing: A Problem Solving Approach*, 3rd ed. (Springer-Verlag, New York, 2001), p. 458.

[28] K. Kondo, O. Ueda, S. Isozumi, S. Yamakoshi, K. Akita, and T. Kotani, IEEE Trans. Electron Devices **ED-30**, 321 (1983).

[29] H. Imai, K. Isozumi, and M. Takusagawa, Appl. Phys. Lett. **33**, 330 (1978).

[30] Y. Horikoshi, T. Kobayashi, and Y. Furukawa, Jpn. J. Appl. Phys. **18**, 2237 (1979).

[31] Y.S. Fatt, IEEE J. Quantum Electron. **27**, 30 (1991).

[32] R.L. Scheaffer and J.T. McClave, *Probability and Statistics for Enginners*, 3rd ed. (PWS-KENT, Boston, 1990), p. 327.

[33] S.L. Chuang, A. Ishibashi, S. Kijima, N. Nakayama, M. Ukita, and S. Taniguchi, IEEE J. Quantum Electron. **33**, 970 (1997).

[34] S.K.K. Lam, R. Mallard, D.T. Cassidy, J. Appl. Phys. **94**, 1803 (2003).

[35] T. Kobayashi and Y. Furukawa, IEEE J. Quantum Electron. **QE-15**, 674 (1979).

[36] Y.S. Fatt, IEEE J. Quantum Electron. **27**, 30 (1991).

[37] Y. Horikoshi, T. Kobayashi, and Y. Furukawa, Japan. J. Appl. Phys. **18**, 2237 (1979).

[38] L.A. Coldren and S.W. Corzine, Diode Lasers and Photonic Integrated Circuits (John Wiley & Sons, New York, 1995), ch. 2.

[39] T.A. DeTemple and G.M. Herzinger, IEEE J. Quantum Electron. **29**, 1246 (1993).

[40] Chu, S.N.G., A. Katz, T. Boone, P.M. Thomas, V.G. Riggs, W.C. Dautremont-Smith, and W.D. Johnston, Jr., J. Appl. Phys. **67**, 3754 (1990).

[41] Stareev, G., H. Kunzel, and G. Dortmann, J. Appl. Phys. **74**, 7344 (1993).

[42] Seki, S., H. Oohasi, H. Sugiura, T. Hirono, and K. Yokoyama, J. Appl. Phys. **79**, 2192 (1996).

[43] H. Asahi, M. Fukuda, Y. Kawamura, Y. Noguchi, and H. Nagai, J. Appl. Phys. **55**, 656 (1984).

[44] B.R. Frieden, *Probability, Statistical Optics, and Data Testing: A Problem Solving Approach*, 3rd ed. (Springer-Verlag, New York, 2001), p. 458.

[45] N. Yamada, G. Roos, and J. S. Harris, Jr., Appl. Phys. Lett. **59**, 1040 (1991).

[46] M. Fukuda, Reliability and Degradation of Semiconductor Lasers and LEDs (Artech House, Boston, 1991), p.300.

[47] G. Zhang, J. Nappi, A. Ovtchinnikov, H. Asonen, and M. Pessa, J. Appl. Phys. **72**, 3788 (1992).

[48] J. Werner, E. Kapon, A.C. Von Lehmen, R. Bhat, E. Colas, N.G. Stoffel, and S.A. Schwarz, Appl. Phys. Lett. **53**, 1693 (1988).

[49] M. Jalonen, M. Toivonen, P. Savolainen, J. Kongas, and M. Pessa, Appl. Phys. Lett. **71**, 479 (1997).

[50] E.I. Gordon, F.R. Nash, R.L. Hartman, IEEE Electron Dev. Lett. **EDL-4**, 465 (1983).

[51] F.R. Nash, W.J. Sundburg, R.L. Hartman, J.R. Pawlik, D.A. Ackerman, N.K. Dutta, and R.W. Dixon, AT&T Tech. J. **64**, 809 (1985).

[52] F.R. Nash, W.B. Joyce, R.L. Hartman, E.I. Gordon, and R.W. Dixon, AT&T Tech. J. **64**, 671 (1985).

[53] R.L. Hartman and R.W. Dixon, Appl. Phys. Lett. **26**, 239 (1975).

[54] W.B. Joyce, K.Y. Liou, F.R. Nash, P.R. Bossard, and R.L. Hartman, AT&T Tech. J. **64**, 717 (1985).

[55] R.L. Scheaffer and J.T. McClave, *Probability and Statistics for Enginners*, 3rd ed. (PWS-KENT, Boston, 1990), p. 327.

[56] P. D. Colbourne and D. T. Cassidy, IEEE J. Quantum Electron. **29**, 62 (1993).

[57] D. T. Cassidy, S. K. K. Lam, B. Lakshimi, D. M. Bruce, Appl. Opt. (submitted).

[58] R. A. Gottscho, B. L. Preppernau, S. J. Pearton, A. B. Emerson, and K. P. Giapis, J. Appl. Phys. **68**, 440 (1990).

[59] S. D. Lester, T. S. Kim, and B. G. Streetman, J. Appl. Phys. **60**, 4209 (1986).

[60] S. D. Lester, T. S. Kim, and B. G. Streetman, J. Electrochem. Soc. **133**, 2208 (1986).

[61] H. Nagai, S. Tohno, and Y. Mizushima, J. Appl. Phys. **50**, 5446 (1979).

[62] T. Suzuki and M. Ogawa, Appl. Phys. Lett. **34**, 447 (1979).

[63] H. Nagai, Y. Noguchi, J. Appl. Phys. **50**, 1544 (1979).

[64] H. Nagai, Y. Noguchi, Appl. Phys. Lett. **33**, 312 (1978).

[65] C. S. Liu and J. F. Kauffman, Appl. Phys. Lett. **66**, 3504 (1995).

[66] S. D. Offsey, J. M. Woodall, A. C. Warren, P. D. Kirchner, T. I. Chappell, and G. D. Pettit, Appl. Phys. Lett. **48**, 475 (1986).

[67] D. L. Lile, *Physics and Chemistry of III-V Compound Semiconductor Interfaces*, C. W. Wilmsen, ed. (Plenum Press, New York, 1985), p. 332.

[68] C. J. Spindt and W. E. Spicer, Appl. Phys. Lett. **55**, 1653 (1989).

[69] H. Hasegawa, H. Ishii, T. Sawada, T. Saitoh, S. Konishi, Y. Liu, and H. Ohno, J. Vac. Sci. Technol. **B6**, 1184 (1988).

[70] I. H. Campbell and P. M. Fauchet, Appl. Phys. Lett. 57, 10 (1990).

[71] D. Guidotti and H. J. Hovel, Appl. Phys. Lett. 53, 1411 (1988).

[72] M. Y. A. Raja, S. R. J. Brueck, M. Osinski, and J. Mclnerney, Appl. Phys. Lett. **52**, 625 (1988).

[73] D. Guidotti, E. Hasan, H. J. Hovel, and M. Albert, Appl. Phys. Lett. **50**, 912 (1987).

[74] A. P. Jacob, Q. X. Zhao, M. Willander, F. Ferdos, M. Sadeghi, and S. M. Wang, J. Appl. Phys. **92**, 6794 (2002).

[75] E. Yoon, R. A. Gottscho, V. M. Donnelly, and H. S. Luftman, Appl. Phys. Lett. **60**, 2681 (1992).

[76] J. C. Fan, C. H. Chen, and Y. F. Chen, Appl. Phys. Lett. **72**, 1605 (1998).

[77] A. Hamed, Phys. Rev. B **44**, 5585 (1991).

[78] D. Redfield and R. H. Bube, Appl. Phys. Lett. **54**, 1037 (1989).

[79] W. B. Jackson, J. M. Marshall, and M. D. Moyer, Phys. Rev. B **39**, 1164 (1989).

[80] R. H. Bube, *Photoconductivity of Solids* (John Wiley & Sons, Inc., New York, 1960), chap.9.

[81] P. A. Tobias and D. C. Trindade, *Applied Reliability* (Van Nostrand Reinhold, New York, 1986), chaps. 5 and 6.

[82] W.W. Daniel, *Applied Nonparametric Statistics*, 2nd ed. (PWS-KENT, Boston, 1990), chap. 3.

[83] W.W. Daniel, *Applied Nonparametric Statistics*, 2nd ed. (PWS-KENT, Boston, 1990), p. 508.

[84] M.A. Fritz, S.K.K. Lam, and D.T. Cassidy, Electron. Lett. (submitted).